

# FE Analyses of Corrosion-Damaged RC Beams Strengthened with FRP Components

Master's Thesis in Structural Engineering

Omar Darwish and Akash Roshan

---

Department of Architecture and Civil Engineering  
CHALMERS UNIVERSITY OF TECHNOLOGY  
Master's Thesis ACEx30  
Gothenburg, Sweden 2022



MASTER'S THESIS ACEX30

# FE Analyses of Corrosion-Damaged RC Beams Strengthened with FRP Components

*Master's Thesis in the Master's Programme Structural Engineering and Building Technology*

Omar Darwish

Akash Roshan



Department of Architecture and Civil Engineering  
*Division of Structural Engineering*  
*Research group: Concrete Structures*  
CHALMERS UNIVERSITY OF TECHNOLOGY  
Göteborg, Sweden 2022

FE Analyses of Corrosion-Damaged RC Beams Strengthened with FRP Components

Omar Darwish

Akash Roshan

Supervisor: Professor Karin Lundgren, Department of Architecture and Civil Engineering and  
Mattias Blomfors, Norconsult AB

Examiner: Professor Karin Lundgren, Department of Architecture and Civil Engineering

Department of Architecture and Civil Engineering  
Division of Structural Engineering  
Concrete Structures Research Group  
Chalmers University of Technology  
SE-412 96 Gothenburg, Sweden

## Abstract

Concrete is one of the most common construction materials used worldwide. The service life of concrete structures is typically limited by deterioration due to corrosion of reinforcement. Therefore, the need for strengthening corrosion-damaged structures has increased in the last decades. Strengthening using Fibre Reinforced Polymers (FRP) is one among many methods that can restore the strength and extend the service life of sound Reinforced Concrete (RC) structures. The effect of FRP strengthening on corrosion-damaged RC structures raised increased research efforts the latest years. The effectiveness of this method on strengthening and repair of corrosion-damaged RC beams was studied in this thesis. The flexural behavior of two beam geometries with several variations of the strengthening system was investigated using non-linear finite element analyses (NLFEA). Corrosion damages were modelled along the whole tensile bars and a horizontal corrosion-induced crack was modelled at the level of the tensile bars along the whole width and the length of the beams. Three FRP components were used for strengthening: FRP plate, inclined U-jackets, and vertical U-jackets with the same FRP arrangement chosen for the studied beam geometries. It was found that the addition of FRP plate to the beam soffit was effective to increase the load-bearing capacity of the beams significantly. When the inclined U-jackets were added to the beams along with the FRP plate, the failure at the FRP plate end close to the supports was prevented, and some additional load-bearing capacity was obtained. However, the increase in load-bearing capacity varied due to factors such as the beam geometry as well as the arrangement, inclination, and dimension of the inclined U-jackets. The addition of vertical U-jackets did not improve the flexural behaviour of the beams when they were placed in the mid-span region. Although, the addition of the vertical U-jackets close to the supports at the location of the failure, resulted in an increase in load-bearing capacity. Furthermore, the effect of including the horizontal corrosion-induced crack in modelling of one of the beam geometries was investigated. No significant influence was observed in the flexural behaviour, except for the beam strengthened with just the FRP plate. From the results of this analysis, it was shown that the presence of the horizontal corrosion-induced crack provoked delamination failure. To further study the effectiveness of FRP strengthening, different FRP arrangement on different beam geometries need to be investigated. Moreover, it would be of interest to study their effectiveness of this method on different RC elements such as slabs and continuous beams.

## **Acknowledgements**

We would like to express our sincere gratitude to our supervisor and examiner, Professor Karin Lundgren for her guidance and support throughout our Master's Thesis. She was really motivating and encouraging which pushed us to work more and obtain more meaningful results than initially planned. Her constructive criticism and comments helped us structure our report in a much better way than we could have possibly imagined.

Our heartfelt gratitude towards Mattias Blomfors for his supervision from the company Norconsult AB, who was very much available any time to clarify our doubts regarding the FE program in addition to his guidance along the way.

We are also very thankful to our opponents Rebecka Philipsson Franzen and Tarek Altoubah for reviewing our project and providing feedback on our work.

We would also like to thank our families and friends that supported us and filled us with the courage and energy needed to reach our goal and complete our thesis.

# Contents

Abstract.....	V
Acknowledgements.....	VI
1. Introduction.....	1
1.1 Background.....	1
1.2 Aim and Objectives.....	2
1.3 Limitations .....	2
1.4 Methodology.....	3
2. Strengthening of RC structures.....	4
2.1 Strengthening using FRP in general .....	4
2.2 Failure modes.....	7
2.2.1 Concrete crushing .....	8
2.2.2 FRP rupture.....	8
2.2.3 Shear failure.....	9
2.2.4 Debonding of FRP laminates .....	9
2.3 Structural effects of corrosion.....	10
2.3.1 The mechanism of corrosion.....	10
2.3.2 Mechanical properties of corroded reinforcement.....	11
2.3.3 Corrosion-induced cracks .....	12
2.3.4 Bond between concrete and corroded reinforcement.....	13
2.3.5 Mechanical behaviour of corroded RC beams.....	14
2.4 Strengthening of corrosion-damaged RC structures using FRP .....	14
3. Design of case studies.....	16
3.1 Influencing parameters for a simply supported RC beam with FRP configurations .....	16
3.2 Selection of analyzed cases.....	17
3.3 Overview of the investigated beams .....	19
3.3.1 Beam geometries.....	19
3.3.2 FRP arrangement .....	20
3.3.3 Pre-loading and corrosion-induced cracks.....	21
3.3.4 Corrosion damages on rebars.....	21
3.3.5 Load application.....	22

4.	NLFEA of the investigated beams .....	23
4.1	Description of FE-models .....	23
4.2	Modelling of RC beams .....	24
4.3	Material properties for concrete .....	26
4.4	Material properties for steel .....	27
4.5	Loading and support plates .....	27
4.6	Interaction between concrete and reinforcement .....	28
4.7	FE mesh .....	29
4.8	Modelling of pre-loading cracks .....	30
4.9	Modelling of corroded reinforcement bars .....	32
4.10	Modelling of FRP strengthening.....	32
4.11	Load steps and convergence criteria .....	34
5.	Results of NLFEA.....	35
5.1	Subcase A-C with corrosion-induced crack.....	35
5.1.1	Non-strengthened beam (A-C-NF) .....	36
5.1.2	Beam strengthened with FRP plate (A-C-P).....	37
5.1.3	Beam strengthened with FRP plate and inclined U-jackets (A-C-P-IU) .....	38
5.1.4	Beam strengthened with all FRP components (A-C-P-IU-U) .....	39
5.2	Subcase A-NC without corrosion-induced crack.....	40
5.3	Case B .....	41
5.3.1	Non-strengthened beam (B-C-NF) .....	42
5.3.2	Beam strengthened with FRP plate (B-C-P).....	43
5.3.3	Beam strengthened with FRP plate and inclined U-jackets (B-C-P-IU) .....	44
5.3.4	Beam strengthened with all FRP components with vertical U-jackets only near the supports (B-C-P-IU-SU) .....	44
5.3.5	Beam strengthened with all FRP components (B-C-P-IU-U).....	45
6.	Discussions .....	46
7.	Conclusions and suggestions for further investigations.....	48
7.1	Conclusion .....	48
7.2	Further investigation .....	49
8.	References .....	50
9.	Appendix.....	I
	Appendix A: Material properties of reinforcement .....	I

Appendix B: Pre-loading and corrosion-induced cracks .....	II
Appendix C: Corrosion modelling.....	IV
Appendix D: FRP properties.....	V
Appendix E: Hand calculation for Case B .....	VI

# 1. Introduction

## 1.1 Background

Concrete is one of the most common construction materials used in many countries. It has been and will continue to be of high importance for different types of construction across the world [1]. Concrete structures are expected to fulfil the demands of having a service life of about 100-120 years. The service life of reinforced concrete structures is affected significantly by deterioration due to corrosion of reinforcement, abrasion, chemical attack, alkali-aggregate reaction, cracking and with cyclic freezing and thawing. All of these reduces the durability of the concrete structures [2].

Corrosion of steel is the most significant durability issue for Reinforced Concrete (RC) structures [3]. Chloride-induced and carbonation-induced corrosion are the main causes for the degradation of mechanical properties of RC members. They cause reduction in cross-sectional area of rebars, cracking, spalling and loss of bond strength [4]. As consequence, reduction in load-carrying, deformation capacity, and flexural stiffness will take place [3], [5].

The need for repair of existing buildings has increased in the last decades. Financial constraints create a strong incentive to come up with cost-effective methods to extend the service life of a structure. Repairing or upgrading a building is usually cheaper than constructing a new building given the functions are met after the repair [6]. Furthermore, extending the service life of an existing structure reduces the extraction of natural resources and has a positive impact on the environment in terms of reduced pollution and utilization of resources [6], [7]. Also considering the time of action, it is quicker to repair an existing building than build a new one. Moreover, it is often possible that the building can be used during the repair operation [6]. The repair work is normally carried out with an intention to enhance the performance of the building in terms of load-carrying capacity, durability, or aesthetics. To extend the service life, or to increase the capacity of concrete structures, several methods can be implemented, such as patch repair, externally bonded steel plates, treatment with chemicals and resins, grouting, and, using Fibre Reinforced Polymers (FRP) [1], [8]. Concerning corrosion damage, patch repair was commonly used to restore the serviceability of cracked concrete structures [9]. Patch repair involves removal of concrete cover until the corroded reinforcement layer and replacing it with a new layer of concrete. When patch repair was carried out before bonding the FRP laminates, it proved to have limited benefits with regards to increasing the deformation capacity, and the ultimate load-carrying capacity [7], [10]. Also, this method was uneconomical for short term extension of service life in refurbishment. Hence, it is of interest to further investigate other strengthening methods such as FRP strengthening on corrosion-damaged RC structures.

Based on an experimental study by Yang [8], [11], using FRP for strengthening RC structures has proven to be an efficient method when the members were subjected to corrosion damage. Three different types of beams were investigated, one without strengthening, and the other two beams strengthened with CFRP (Carbon Fibre Reinforced Polymer) and GFRP (Glass Fibre Reinforced

Polymer). The FRP components used for strengthening the beams were FRP laminates, inclined U-jackets close to the supports and vertical U-jackets. Finite Element Analysis (FEA) of these experiments was carried out by Franklin and Gotame [11], [12]. These showed similar results in comparison; thus, the modeling method was validated. Their analyzes were focused on a certain beam geometry, corrosion damages, and FRP arrangement according to the experiments. To study the effectiveness of the strengthening method, they suggested further investigations be performed by changing beam dimension, corrosion pattern and FRP arrangement. This Master's Thesis can be viewed as continuation of their work.

## **1.2 Aim and Objectives**

The aim of this Master's Thesis was to evaluate the effectiveness of FRP strengthening of beams, subjected to reinforcement corrosion damage. The study is focused on the flexural response and FEA was used for investigations. To achieve the goals of this thesis, the following objectives were set up:

- Design a parameter study to investigate the influence of different parameters on FRP strengthened RC beams.
- Perform the parameter study using non-linear finite element modelling of beams that are subjected to corrosion damage and strengthened by FRP.
- Investigate the flexural response and the effectiveness of the individual FRP components.

## **1.3 Limitations**

The limitations of this Master's Thesis work are:

- The main focus was on studying the flexural response of beams.
- This study was performed on simply supported beams with a rectangular cross-section. Thus, techniques for strengthening slabs or columns were not included.
- The work in this Master's Thesis was carried out using FEA, thus no experimental work was conducted.

## **1.4 Methodology**

A review of existing literature was carried out to have a better understanding of the effects of corrosion damage on reinforced concrete structures. Based on this, a parameter study was designed to investigate the influence of different parameters on the flexural response of beams. Non-linear Finite Element Analyzes (NLFEA) were used to investigate strengthened beams with corroded reinforcement using the software DIANA FEA 10.5. The modelling procedure from Franklin and Gotame [12] was used as a reference for the modelling of beams. The results were evaluated and guidance on strengthening, and repair of corrosion damaged RC beams was provided.

## 2. Strengthening of RC structures

### 2.1 Strengthening using FRP in general

The traditional methods for strengthening concrete structures involve increasing the cross-sectional area, post-tensioning, traditional casting with new reinforcement, shotcreting, steel jacketing, etc. Such methods have proven to be effective in the past and are assured to work in the future as well. In the mid-70s, a strengthening method using steel plates glued to the surface of the concrete structures was pioneered. This method was a common practice in Central Europe as well as in the USA and Japan. Sweden has reinforced about 15-20 bridges using this technology [6]. However, this method has several disadvantages; the steel plates are heavy to mount and prone to corrosion, the need for splice plates between the reinforcement plates, difficulties with regards to mounting on curved surfaces like pillars etc. In the late 1980s, Japan started investigating the possibilities of strengthening concrete structures using FRP. It was applied first on chimneys and pillars with regards to earthquake stresses using traditional hand laying methods. Hence it was during this period that the use of composite materials like FRP for reinforcement came into existence. As a result of further investigations and experiments, this type of strengthening method has turned out to be common and accepted throughout the world [6].

A polymer composite material consists of fibres, that could be continuous or short, that are placed and held in a polymer matrix. The fibre material is usually made of glass (GFRP), aramid, or carbon (CFRP) while the matrix material is thermosetting plastic such as epoxy or vinyl ester [6], [13]. The most common combination of FRP is using CFRP with epoxy matrix. The properties of fibre, matrix, contact layer, and fibre orientation will influence the mechanical properties of the composite material. The volume of fibre in FRP can vary between 35-75% depending on several factors such as manufacturing process, desired material properties, and material selection of fibre or matrix. The composite material is usually attached by gluing it to the surface of the concrete or sometimes embedded in grooves in the concrete cover as well. Before gluing the FRP laminates, preparatory work is to be carried out on the concrete surface which usually involves sanding and blasting in order to obtain better adhesion. Proper care must be taken to avoid gluing on wet surfaces or at low temperatures. It can also be attached mechanically to the concrete surfaces without glue using fasteners [6].

FRP is composite material with properties such as high strength, corrosion resistance and low weight. These properties will make it an efficient material to strengthen building components. As shown in Figure 1, FRP material has higher ultimate capacity than steel. The stress-strain relationship for FRP is expressed by a linear elastic response until the breaking point ( $\epsilon_{fu}$ ), whereas mild steel exhibits elastic response only until yielding and undergoes plastic deformation until steel rupture when the ultimate strain is reached ( $\epsilon_{su}$ ).

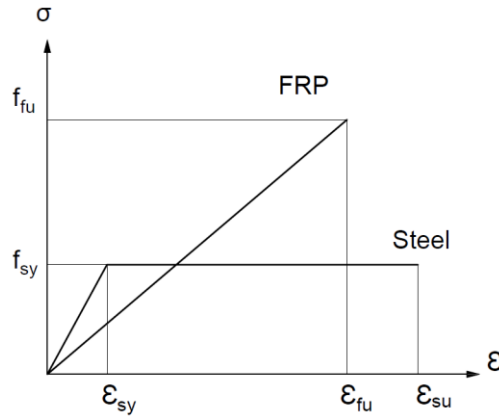


Figure 1: A comparison of stress-strain relationship between steel and FRP, redrawn from [6].

The mechanical properties of FRP are influenced by different parameters which include the properties of the matrix, the properties of the fibres, orientation of the fibres in the matrix, and the manufacturing process. As the fibres have low compressive strength and high tensile strength, the FRP composites will show similar traits. The strength and stiffness are direction dependant and completely dominant in the direction along which the fibres are oriented. If the direction of the force deviates by  $30^\circ$  from the direction of fibres, a reduction in the tensile strength is observed which is about 70% for CFRP and 35% for GFRP [6]. Because of this reduction, FRP components are available in bi-axial and tri-axial systems where the fibres are oriented along different directions. These kinds of systems are most often used in the construction industry. However, having FRP sheets with inclination of  $45^\circ$  near the supports will prevent the propagation of shear crack and result in better utilization of FRP strengthening [13]. Figure 2 shows an example of U-jackets inclined at an angle of  $45^\circ$ . Another aspect that considerably changes the material property of the matrix is the temperature. Hence it is important to fireproof the elements strengthened using FRP composites by coating the FRP with a protective layer of ceramic, adding flame retardants in the resins or using char-forming resins [14].

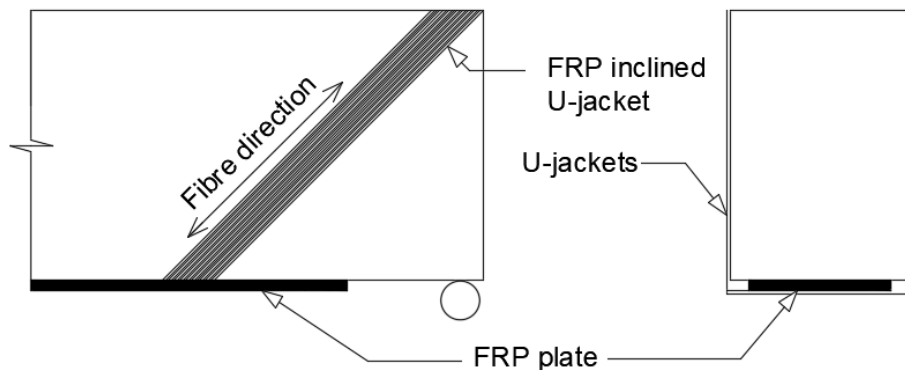


Figure 2: The orientation of the inclined U-jackets at the supports, redrawn from [15].

Figure 3 shows the stress and strain distribution over the cross-section of a reinforced concrete beam strengthened with FRP sheets on the bottom surface of the beam. In Figure 3b, the dotted line represents the strain distributions before strengthening and when the beam is loaded in the serviceability limit, where  $(\epsilon_{co})$  is the compressive strain and  $(\epsilon_{uo})$  is the tensile strain on the top and bottom surface of concrete respectively. The solid line in Figure 3b represents the strain distributions after strengthening and when the beam is loaded to the ultimate limit state, where  $(\Delta\epsilon_c)$  is the additional compressive strain in concrete. On the tensile surface of the beam, it can be observed that there is an increase in strain  $(\epsilon_f)$  in the section after the addition of FRP in the ultimate limit state. Also, the neutral axis is slightly shifted downwards. At stage III, there is full utilization of the constituent materials, and a stress block is developed as shown in Figure 3c. This can be simplified as shown in Figure 3d for design calculations and sectional analysis [6].

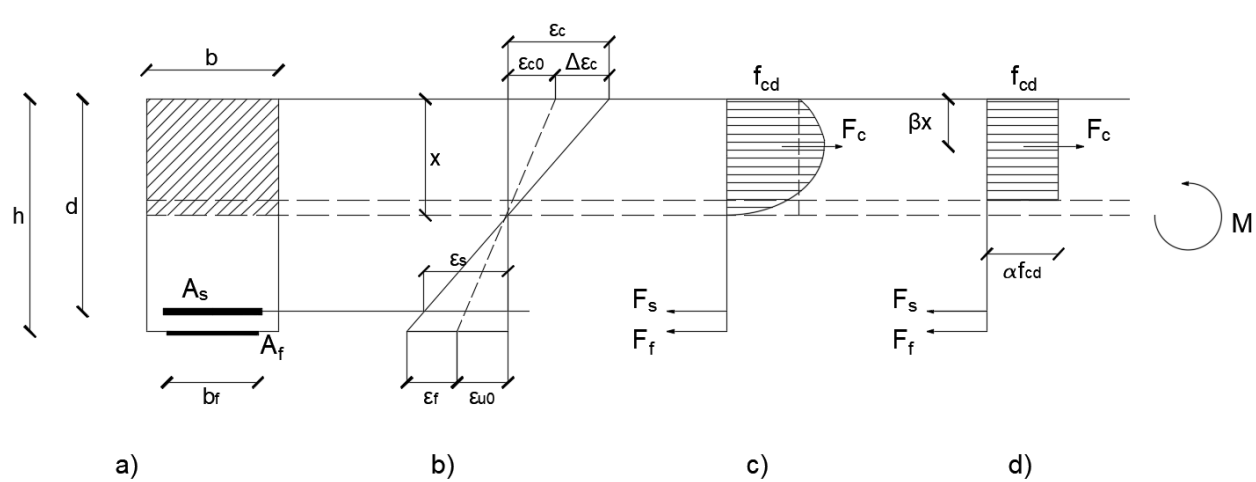


Figure 3: Stress distribution over a concrete section before and after strengthening redrawn from [6].

Many experiments were carried out in the past 100 years that provided the basic design recommendation for RC structures that is used today. However, the research and development behind the use of composite material such as FRP has considerably increased only in the last three decades [6], [16]. Today, FRP has proven to be a promising strengthening material. But there are yet no standards to follow in order to design and dimension FRP to strengthen RC structures. Designers and stakeholders that want to use FRP, usually follow some guidelines provided by material suppliers that help to estimate the required amount of FRP. To make this estimation for a beam, the required area of FRP is calculated based on the moment capacity to be achieved. The moment capacity can be calculated according to [6]:

$$M_d \approx 0.9(A_s \epsilon_s E_s d + A_f \epsilon_f E_f h) \quad (2.1)$$

where  $A_s$  is reinforcement area,  $f_y$  is the yield strength of the reinforcement,  $\varepsilon_{fu}$  is rupture strain and  $E_f$  is Elastic modulus of FRP whereas  $d, h$  are presented in Figure 3. The area of FRP needed for the design moment capacity is found by rearranging Equation 2.1.

$$A_f \approx \left( \frac{M_d}{0.9} - A_s \varepsilon_s E_s d \right) / (\varepsilon_f E_f h) \quad (2.2)$$

## 2.2 Failure modes

Flexural, shear, or anchorage failure are the main failure modes for FRP strengthened RC beams. They can occur depending on if composite action between concrete and FRP or between concrete and reinforcement is maintained. The types of flexural failure when concrete-FRP and concrete-reinforcement composite action is maintained are: (1) Concrete crushing, (2) FRP rupture (3) Rebar rupture. If not, other types of failure can occur at the end or at the mid-span in terms of debonding of FRP laminates, separation of concrete due to cracking or anchorage failure [17]. They can be further categorised as follows: (4) Plate end interfacial delamination (5) Concrete cover separation (6) Flexure crack delamination (7) Shear crack delamination (8) Anchorage failure of main reinforcement. When the section does not have sufficient shear capacity the beam fails due to (9) Shear failure. The possible failure modes are illustrated in Figure 4.

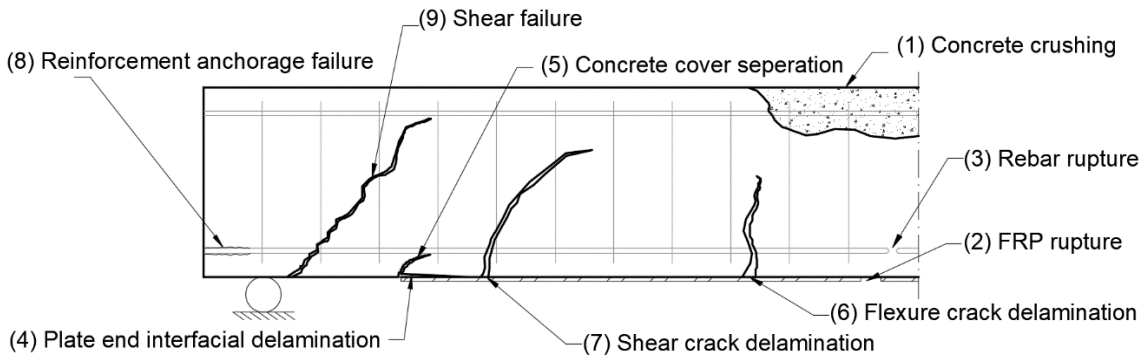


Figure 4: Different failure modes of FRP strengthened RC beams redrawn from [18].

## 2.2.1 Concrete crushing

The strength of RC beams is highly dependent on the reinforcement ratio whilst varying this will result in a different failure mode. A heavily reinforced beam will usually fail due to concrete crushing in the compressive zone as shown in Figure 5, whereas this failure mode is unlikely when the beam is lightly reinforced. In addition, heavily reinforced beams will show a decrease in the utilization of the tensile capacity of FRP [19]. Similarly, over-strengthening with FRP will also lead to concrete crushing. This kind of failure should be avoided to prevent brittle behaviour of the beam.

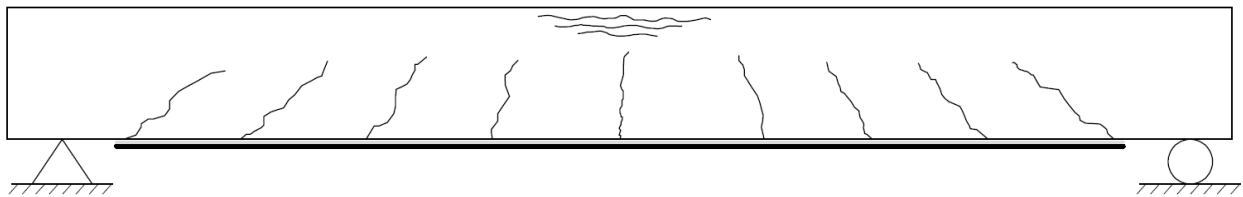


Figure 5: Failure due to concrete crushing redrawn from [19].

## 2.2.2 FRP rupture

This type of failure occurs when the rupture strain of FRP is exceeded, see Figure 6. The thickness of FRP is an important parameter to be considered as increasing the thickness may switch the failure mode from FRP rupture to any other failure modes [20].

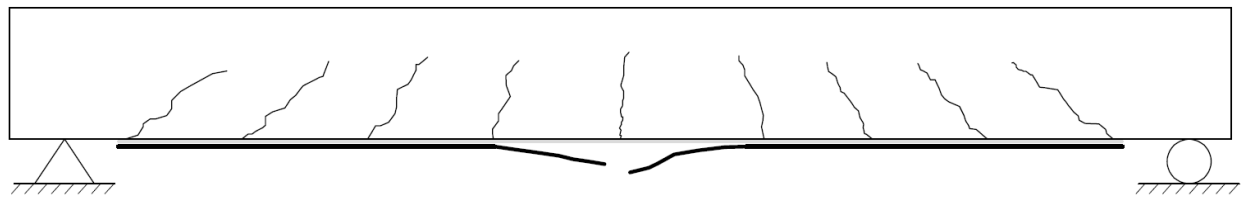


Figure 6: Failure due to FRP rupture redrawn from [19].

### **2.2.3 Shear failure**

The reinforced concrete beam will undergo shear failure before flexural failure if the section does not have sufficient shear capacity. Furthermore, the type and the position of loading largely influences the moment/shear relationship as concentrated loads closer to the supports causes higher risks for shear failure. This type of failure can be observed when the beam is strengthened using FRP bonded laminates and the shear capacity is reached prior to bending failure [17]. Corrosion of longitudinal rebars will affect the shear capacity of the beam as it reduces the bond strength, reduces the dowel action, and the stiffness of the beam. As the bond strength between concrete and longitudinal rebars is affected, a transition in the load-carrying mechanism is observed [17], [21]. Shear reinforcement/stirrups undergo corrosion before the main rebars as they are closer to the concrete surface and are usually smaller in diameter than the longitudinal bars [22]. Hence, a reduction in the shear capacity with the reduction in the cross-sectional area of the rebars is noted [22], [23]. This can lead to brittle failure of the structures that have been designed to carry the shear forces through the stirrups.

### **2.2.4 Debonding of FRP laminates**

Failure that occurs when the FRP gets delaminated from the beam is known as failure due to debonding of FRP. This failure mode can be further classified into two types based on the location along the beam: 1) End debonding 2) Mid-span debonding. The end debonding originates closer to the end of the laminate and then progresses along the tensile reinforcement or near the bond line between FRP and concrete. As a result, two failure modes can take place, plate-end interfacial debonding or concrete cover separation at the end of FRP plate, respectively [19], see Figure 7. The mid-span debonding failure can occur because of flexural cracking (flexure crack delamination) or inclined flexural-shear cracking (shear crack delamination) which progresses towards the ends parallel to the concrete/adhesive interface. Flexural crack delamination is likely to occur when the beam is lightly reinforced in the presence of large flexural cracks. It is also likely to occur when the beam is notched, or when corrosion pits are observed on the tensile reinforcement. Although, shear crack delamination is more critical as the failure is very brittle [18].

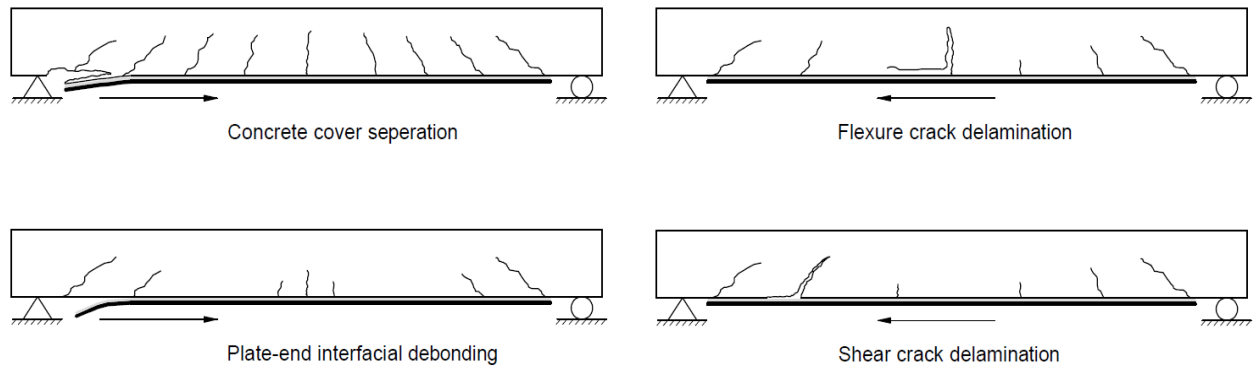


Figure 7: FRP debonding failures redrawn from [19].

## 2.3 Structural effects of corrosion

Corrosion has adverse deteriorating effects on the structural behaviour of RC beams. To tackle the problem of corrosion on RC beams and to prevent further damage by strengthening using FRP, it is of importance to have a better understanding of the mechanism of corrosion and along with its effects. Therefore, the structural effects of corrosion on RC beams are presented in this section.

### 2.3.1 The mechanism of corrosion

Corrosion is the main cause of deterioration of RC beams during its service life [24]. Before corrosion takes place, the embedded reinforcement bars are protected by a passivating layer due to the high alkalinity of surrounding concrete. This layer can lose its passivity in two ways; concrete cover carbonation which causes alkalinity loss, or attack of chloride ions at the surface of the steel [25]. Both of these two conditions lead to initiation of corrosion of the reinforcement. In the case of carbonation-induced corrosion, the propagation of corrosion is usually uniform (general corrosion) over the surface of the reinforcement. Meanwhile, chloride-induced corrosion is the main cause of localized corrosion (pitting corrosion) [25], see Figure 8. These two types of corrosion affect the flexural behaviour and the resulting failure mode of RC beams differently. General corrosion decreases the ultimate load-bearing capacity whereas pitting corrosion also affects the deformation capacity of RC beams. As a consequence of corrosion, corrosion-induced cracks are formed in addition to the weakening of the bond between concrete and reinforcement. This will affect the mechanical properties of RC beams.



Figure 8: (a) Pitting corrosion. (b) General corrosion.

### 2.3.2 Mechanical properties of corroded reinforcement

The mechanical properties of reinforcement bars are highly affected by corrosion according to several sources [5], [26], [27]. Both load-carrying and deformation capacity is decreased in varying magnitude depending on corrosion level, rebar diameter and the type of attack. For the same depth of corrosion, the decrease in residual capacity is higher for the case while using smaller rebar diameter [27]. Carbonation and chloride attack cause general corrosion and local pits corrosion, respectively. A higher reduction of rebar cross-sectional area in the position of the pits is observed [26], that lead to high stress concentration and local strain concentration, as illustrated in Figure 9. As a result, the load-carrying and deformation capacity are severely reduced. The reduction also affects the surrounding area of the pits until a certain maximum local corrosion level exceeds a critical local corrosion level. It has been observed that the critical local corrosion level can be calculated as  $1 - \frac{f_y}{f_u}$ , where  $f_y$  is the yield strength and  $f_u$  is the ultimate strength [5].

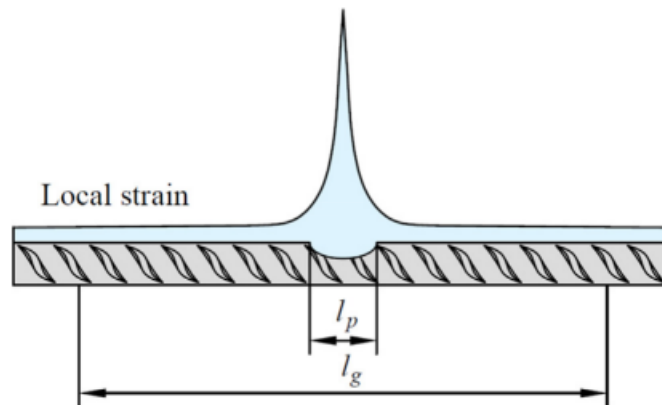


Figure 9: Local strain concentration in the position of the pits. Figure from [5], with permission.

### 2.3.3 Corrosion-induced cracks

Corrosion-induced cracks in RC structures can be explained as the cracking of concrete due to the build-up of splitting tensile stresses caused by the expansive corrosion products. When corrosion is initiated, the corrosion products occupy voids in the porous layer of steel/concrete interface [28]. As the volume of corrosion products is 2-6 times the volume of initial steel [29], increasing expansive pressure is exerted on the surrounding concrete layer with time causing build-up of tensile stresses within the concrete. When the maximum principal tensile stress increases beyond the tensile strength of concrete, cracks are observed at the steel/concrete interface [30]. This corresponds to the cracked state of concrete as shown in Figure 10. The quantity of corrosion products corresponding to this point is called “critical amount of corrosion products” and the loss of cross-section is called “critical attack penetration” [25]. Upon further corrosion of the rebars, the corrosion products accumulate in the steel/concrete interface and cause propagation of cracks [31]. The cracks can either be vertical or horizontal along the direction of the main bars depending on various factors. The cracking pattern is influenced by the rate of corrosion, type of corrosion products, porosity of concrete, concrete cover, diameter of the bars and spacing between the bars [25]. If concrete cover is relatively small in comparison to the rebar spacing, the cracks tend to develop at  $45^\circ$ . Spalling takes place when such cracks grow large enough and reach the surface of concrete as shown in Figure 11. If the spacing is relatively small, the cracking tends to propagate across the plane of the rebars and causes delamination as shown in Figure 11 [25]. These cracks are not visible until they reach the outer surface of the beam. The additional cracks create an easy path for corrosion to propagate and cause further damage [32].

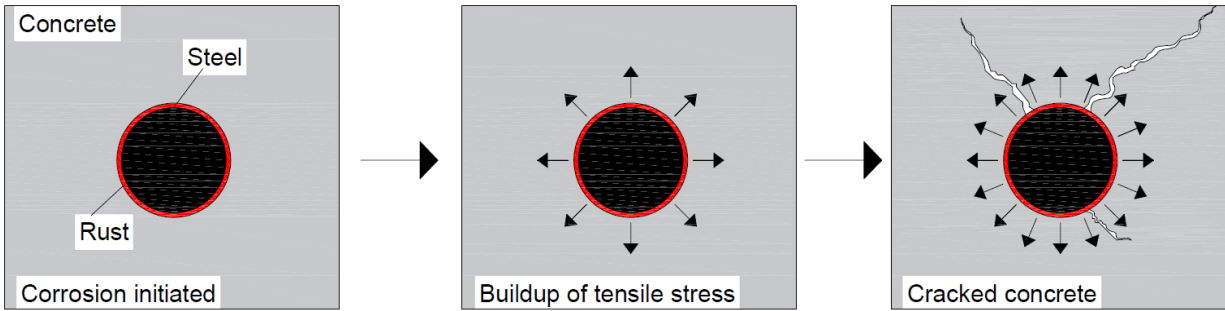


Figure 10: Stages of corrosion-induced cracking redrawn from [25].

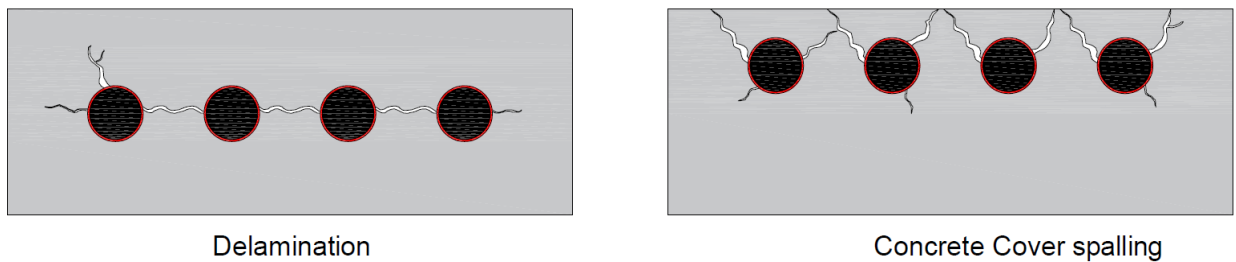


Figure 11: Cracking pattern based on concrete cover depth and rebar spacing redrawn from [25].

### 2.3.4 Bond between concrete and corroded reinforcement

Reinforced concrete elements resist the applied load through composite action between the steel reinforcement and concrete. An efficient bond ensures that the load-carrying and deformation capacities of the element are met. The bond mechanism is influenced by three factors: 1). Mechanical interlock 2). Friction resistance 3). Chemical adhesion [33]. Mechanical interlocking is of large importance for deformed bars whereas chemical adhesion has minor effects. This is because it disappears after the first slippage of rebar resulting in the transfer of load between steel and concrete through interlocking. In general, the factors affecting the bond failure mode are concrete cover thickness, concrete strength, reinforcement geometry and size, reinforcement position, bonded length, transverse pressure and amount of transverse reinforcement [33]. As explained in section 2.3.3, the expanding corrosion products exert expansive pressure which leads to cracking of surrounding concrete. Once cracking is initiated, the bond strength progressively reduces until failure [34]. It is more dangerous in the case where there is no transverse reinforcement as the stirrups can provide additional confinement and keep the cracks small.

### **2.3.5 Mechanical behaviour of corroded RC beams**

Corrosion of reinforcement in RC beams has adverse effect on the flexural and shear behaviour. Apart from loss of flexural strength, corrosion will also cause loss of bond strength between concrete and reinforcement [35], as described in section 2.3.4. Anchorage failure and reduction in shear capacity can be the consequences of having a weakened bond between concrete and the reinforcement. Furthermore, pitting corrosion on the bars will lead to lowering of the moment and shear capacity of the beam locally. Corrosion-induced cracks and spalling of concrete cover contribute to the reduction of flexural strength due to an increment in the number of cracks and the loss of a part of concrete cross-sectional area respectively [25], [31].

### **2.4 Strengthening of corrosion-damaged RC structures using FRP**

The use of FRP composite materials has significantly increased in the past three decades as a promising material that has been proven to be beneficial for repair and rehabilitation of existing structures. It is used as a retrofitting application to increase the performance of the structures or restore the strength that the structure has been designed for [36]. Nevertheless, there are no guidelines on the application of FRP sheets to strengthen RC structures subjected to corrosion damages.

Different FRP components have been implemented or used to repair concrete structures, such as FRP plate laminate, vertical and inclined U-jackets, or a combination of them, see Figure 12. From the results of an experimental study [37], beams strengthened with single continuous FRP sheet along the length between supports showed lowering of ultimate load and deformation capacity compared to the beam strengthened with two smaller segments of FRP sheets nearer to the supports. Thus, an extra addition of FRP sheets in some cases can result in worsening of the flexural performance of the beam. Change of the dimension, amount, and arrangement of FRP could possibly influence the flexural response of RC beams. Several research have investigated the influence of different FRP components on deteriorated RC structures [8], [36], [38], [39], and their results are summarized.



Figure 12: Combination of different FRP components from [8], with permission.

Corroded RC beams usually suffer from decreased flexural performance due to corrosion of longitudinal rebars. The use of externally bonded FRP plates to strengthen corroded RC beams has shown to be an efficient method according to a previous experimental study [8]. A substantial increase in load-carrying capacity and stiffness was observed for beams strengthened with FRP plate at the bottom surface of the beam. Moreover, an addition of inclined U-jackets near supports showed further enhancement in flexural behaviour of the beam [12]. Another study has showed that the use of inclined U-jackets oriented at  $45^\circ$  showed a transition in the failure mode of FRP-plated RC beams from FRP debonding to concrete crushing or FRP rupture [39]. The strengthened beam could carry increased load even after complete debonding of the FRP plate, as the U-jackets remain bonded. Furthermore, the inclined U-jackets lead to a significant increase in the load-carrying capacity and maximum strain of the FRP plate. The magnitude of the additional load that can be carried is governed by the thickness and width of U-jackets [38], [39]. Although, this increase is less significant when the U-jackets are wide enough to cause concrete crushing, and effective bond length is shorter than the bond length of the inclined U-jackets [39].

A different study on U-jackets concluded that the use of U-jackets at the ends of the FRP plate reduces the probability of concrete cover separation failure [38]. This was caused by the reduction of the normal stresses between concrete and FRP plate, and the prevention of horizontal crack propagation at the longitudinal rebar level. Use of sufficiently wide U-jackets prevent concrete cover separation whereas use of narrower vertical U-jackets can only shift the location of it from the plate ends to the inner side of the U-jackets.

### 3. Design of case studies

Taking into consideration the findings and results from various research, the influence of different parameters on the flexural behaviour of beams was compiled. Based on this compilation, case studies were chosen as motivated in Section 3.2. Details of the case studies are given in Section 3.3.

#### 3.1 Influencing parameters for a simply supported RC beam with FRP configurations

The parameters considered can be broadly grouped under beam geometry, material properties, FRP arrangement, corrosion damage, and load application method. These are further described in the following with notes on their expected influence.

- **Beam geometry and material properties:** Change in height and width of the beam, number, and diameter of rebars, and concrete cover thickness will change the cross-sectional properties of the beam. Moreover, a change in span length with the same depth will affect the failure mode as longer beams will have a higher risk of bending failure. Smaller concrete cover will allow for easier penetration of corrosive agents to reach the level of rebars which initiates corrosion leading to reduction of rebar area [25]. As result, the bond strength between concrete and rebar is reduced in addition to the formation of corrosion cracks which can lead to spalling or delamination. Varying these parameters will have a direct influence on the flexural and deformation capacities of the beam. Furthermore, any change in the material properties of concrete, reinforcement or FRP sheets would directly influence the capacity of the beams.
- **FRP arrangement:** Simply supported beams subjected to corrosion damage can be strengthened with different components: FRP plate, inclined U-jackets, and vertical U-jackets. The FRP plate length and width will have a direct influence on the capacity of the strengthened beam [17]. The shape, width, and number of inclined U-jackets near the ends will affect the flexural and shear performance [39]. They prevent horizontal cracks at the level of reinforcement, hinder the development of shear cracks close to the beam soffit plate [40] and transfer the forces from the FRP plate to the supports. The use of vertical U-jackets has no major effect on enhancement of the ultimate capacity, but they improve the ductility of the beam [39], [40]. Change in spacing, and the dimension of vertical U-jackets can influence the deformation capacity of the beam.
- **Corrosion damage:** Corrosion damage is broadly categorized into general corrosion and pitting corrosion. The level of corrosion, the extent of general corrosion along the rebars, depth, length, position, and number of corrosion pits will influence the flexural behaviour and failure mode of the beams. General and pitting corrosion will cause reduction of rebar

cross-sectional area which affects the flexural capacity of beams [41]. The bond-stress relationship between the rebar and concrete is also influenced by the level of corrosion [42]. The deformation capacity of the beam is sensitive to the location, length, and depth of corrosion pits [12]. Corrosion causes cracks, which can lead to concrete spalling or delamination. Furthermore, the bending-induced cracks on the beam allow for an easy path for corrosive agents leading to the formation of pits in those sections [32].

- **Load application method:** Beams strengthened with FRP will show different behaviour when subjected to distributed loads compared to four-point bending loading conditions. An existing literature [17], showed that FRP strengthening is more effective when RC beams are subjected to distributed load.

### 3.2 Selection of analyzed cases

Two different beam geometries were chosen to be analyzed based on the qualitative assessment of the influencing parameters presented in section 3.1. Some of the parameters were assigned constant values whereas some of them were chosen to be varied for the two different beam geometries, see Figure 13.

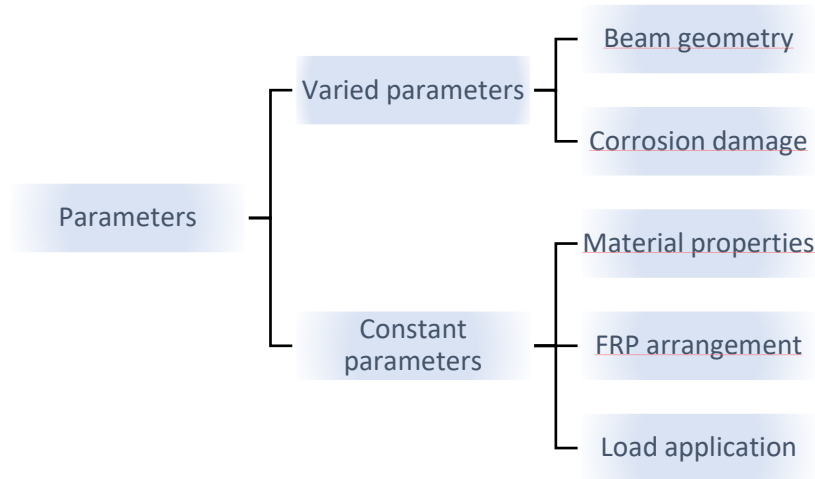


Figure 13: Flowchart showing the choice of parameters.

Material properties and load application were chosen to be kept constant for both cases to obtain comparable results. As the primary goal was to investigate the influence of FRP strengthening method on corroded beams, the effect of corrosion damage on different geometries by keeping the same FRP arrangement was prioritized over material properties and load application.

The beam modelled by Franklin and Gotame [12] had corrosion damages in the middle part of the span. Their analyses showed that FRP plate and inclined U-jackets improved the flexural capacity of the beam, whereas vertical U-jackets had minor impact. Their analysis did neither consider effects of corrosion near the supports, nor the effect of corrosion on the bond stress-slip relationship between concrete and reinforcement. Therefore, it was of interest to investigate the similar beam for the worst-case scenario: when corrosion damage is modelled along complete length of the rebars. With the extension of general corrosion up until the supports, the corrosion-induced cracks were also assumed to be extended along the whole length of the beam in the horizontal plane. In addition, the bond stress-slip relationship for concrete and reinforcement was modified with respect to the level of general corrosion. Then the effectiveness of individual FRP components on the flexural behaviour of the RC beams were studied by adding them in steps starting with FRP plate followed by the inclined U-jackets and then the vertical U-jackets.

As the corrosion-damage with the horizontal corrosion-induced crack could extend along the whole length of the beam, failure due to delamination was the worst-case scenario that could be expected. Therefore, it was of interest to design an alternative beam geometry with a chosen cross-section susceptible to delamination failure and to investigate the effectiveness of FRP strengthening method for such beams. This motivated the design of an alternative geometry. In the following, the two analyzed cases are introduced below, and presented in detail in next subchapter:

**Case A:** The beam geometry and cross section was chosen to be the same as designed by Yang [8] along with the pits on the rebars as chosen by Franklin and Gotame [12]. General corrosion and the horizontal corrosion-induced crack was extended along the whole length of the beam in the horizontal plane. The corrosion level on the rebars and the pre-loading cracks were unchanged.

**Case B:** A wider beam geometry and longer span was assumed. Minimum spacing between reinforcement was chosen to provoke delamination failure. General corrosion and horizontal crack were modelled along the full length of the span. Pre-loading cracks and corrosion pits were assumed which are explained in section 3.3.3 and 3.3.4 respectively.

### 3.3 Overview of the investigated beams

The analyzed RC beams in this thesis were designed based on the study of influencing parameters that are presented in section 3.1 according to the motivations in section 3.2. In this section, the beam geometry, arrangement, and dimension of FRP, material properties, pre-loading and corrosion-induced cracks, corrosion damages on rebars, and load application are presented for both cases.

#### 3.3.1 Beam geometries

The beam geometry for Case A has a span length of 2100 mm, with cross section of 150 x 225 mm, as shown in Figure 14. The beam is reinforced with two tensile and two compressive bars with a clear concrete cover of 24 mm. The main bars have diameters of 12 mm and 10 mm on the tensile zone and compressive zone respectively. Shear reinforcement is provided in the outer region of 750 mm length using two-legged 8 mm stirrups with a spacing of 125 mm.

The span length for Case B was 4200 mm, with a cross section of 500 x 300 mm, as illustrated in Figure 15. Reinforcement ratio was chosen to be the same as for Case A. Two bars of 10 mm diameter were used in the compressive zone whereas, ten bars of 12 mm diameter were used in the tensile zone. The beam was designed to show bending failure by providing sufficient number of stirrups with diameter of 8 mm and spacing of 100 mm.

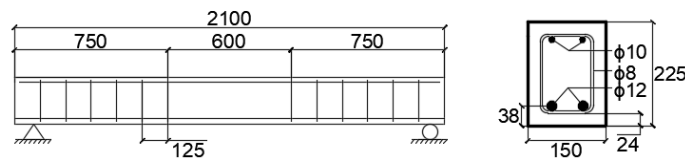


Figure 14: Beam geometry for Case A.

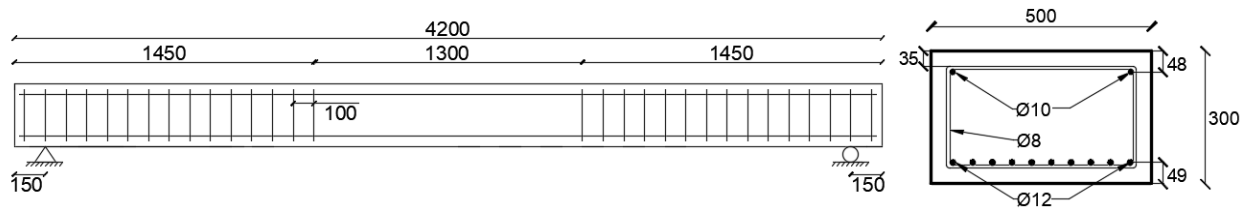


Figure 15: Beam geometry for Case B.

### 3.3.2 FRP arrangement

Three FRP components were attached externally to the RC beams in the following order: i) FRP plate laminate, ii) Inclined U-jackets, iii) Vertical U-jackets. The FRP plate with different dimensions depending on the beam geometry was connected to the beam soffit. Vertical U-jackets were made up of a single layer, whereas the inclined U-jackets consist of a triple layer of FRP. The inclined U-jackets have an inclination of  $45^{\circ}$  and have two sheets crossing each other near the supports. The arrangement of all FRP components for the cases A and B are illustrated in Figure 16 and 17.

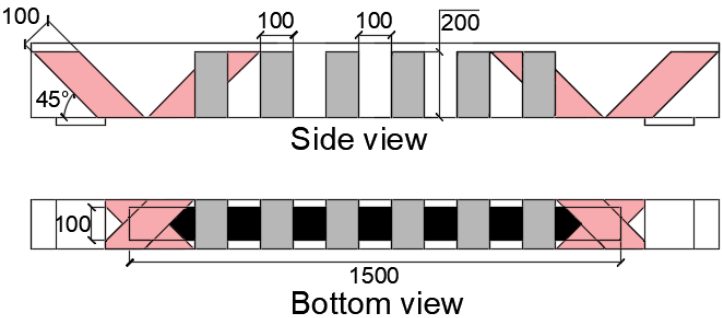


Figure 16: FRP arrangement for Case A.

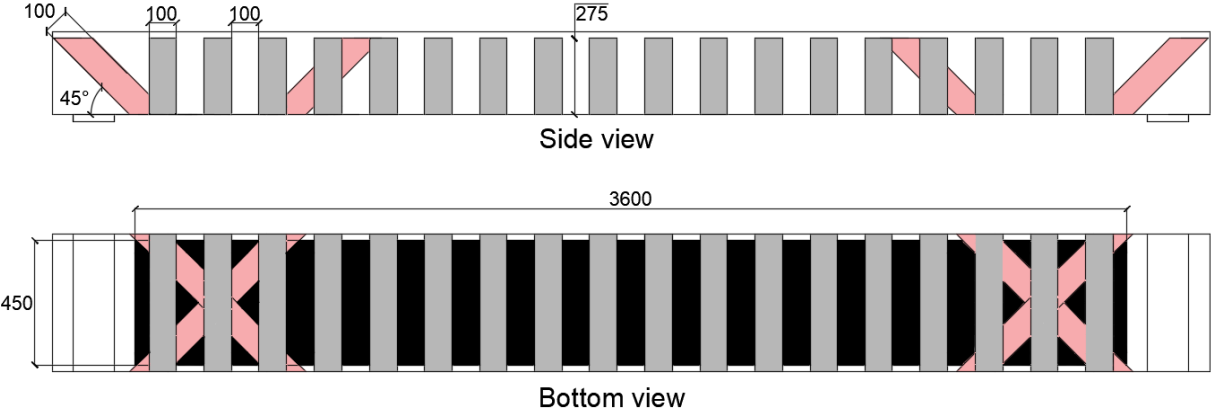


Figure 17: FRP arrangement for Case B.

### 3.3.3 Pre-loading and corrosion-induced cracks

For Case A, the positions of bending and corrosion-induced cracks along the beam were modelled, as documented in the experiment by assuming the same procedure as Franklin and Gotame [12], see Appendix B. In order to further investigate the effect of general corrosion, the horizontal corrosion-induced crack was extended along the whole length of the beam. Figure 18 shows the number and the location of the cracks for Case A.

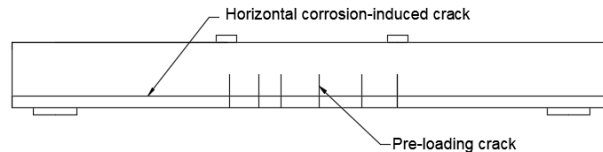


Figure 18: Number and location of the cracks for Case A.

For Case B, the width of pre-loading cracks was calculated according to Eurocode for a service load of  $P_y/1.5$ , where  $P_y$  is the yielding load. This ratio is based on the partial safety factors for imposed load in SLS and ULS. The position of cracks was estimated based on the mean crack band width and the cracks were assumed to be distributed within the length of the span where the cracking moment was exceeded, see Appendix E. The horizontal corrosion-induced crack for Case B was modelled assuming similar properties as modelled in Case A, see Appendix B. Figure 19 shows the location and the number of the cracks for Case B.

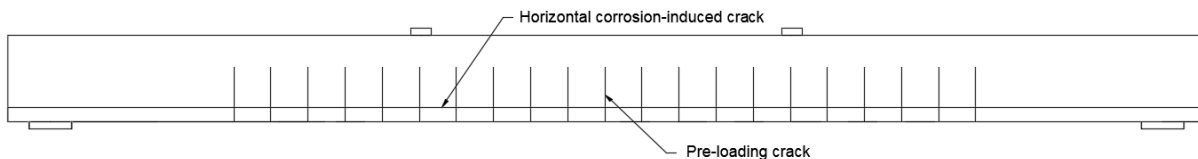


Figure 19: Number and location of the cracks for Case B.

### 3.3.4 Corrosion damages on rebars

The level of corrosion in experiments was measured by Yang [8], using 3D optical scanners by quantifying the cross-sectional area of rebars after corrosion. The average level of general corrosion was measured to be 20 % and this was applied along the whole length of the tensile reinforcement for both Case A and B. Thus, the studied beams have no uncorroded longitudinal tensile bars at any given section. For Case A, the level of corrosion at the pits were taken from Yang [8], whereas the length, position and number of pits were taken as evaluated by Franklin and Gotame [12]. However, for Case B, the length, position, number, and corrosion level for all the

pits were assumed, as there was no experiment conducted on this beam geometry. Therefore, all the pits in Case B were assumed to have the same length and level of corrosion as pit Ib from Case A. Three pits were randomly distributed along each tensile rebar at the location of pre-loading cracks, assuming that the pits were not placed at adjacent cracks along the same rebar. The level of corrosion and position of pits along the rebar are presented in Appendix C. Figures 20 and 21 show the location of the pits along the beam for Case A and Case B respectively.

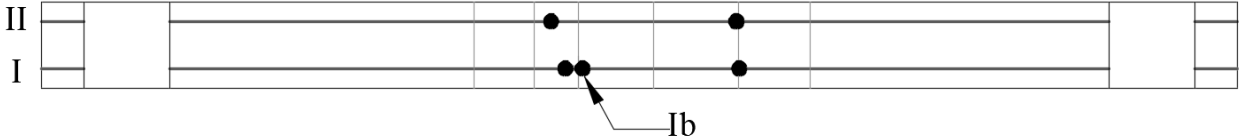


Figure 20: Pits position for Case A.

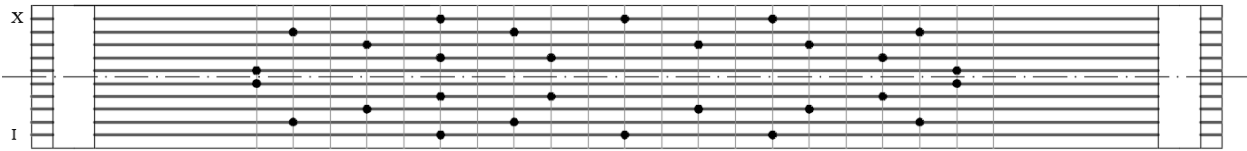


Figure 21: Pits position for Case B.

### 3.3.5 Load application

The beams in the analyses were subjected to four-point bending, increasing the load until failure. The load was applied in terms of deformation-controlled loading at the centre of a loading beam which transfers the load to the beam via loading plates. Loading plates are used to avoid stress concentration on the concrete beams [12]. An illustration of loading is presented in Figure 22.

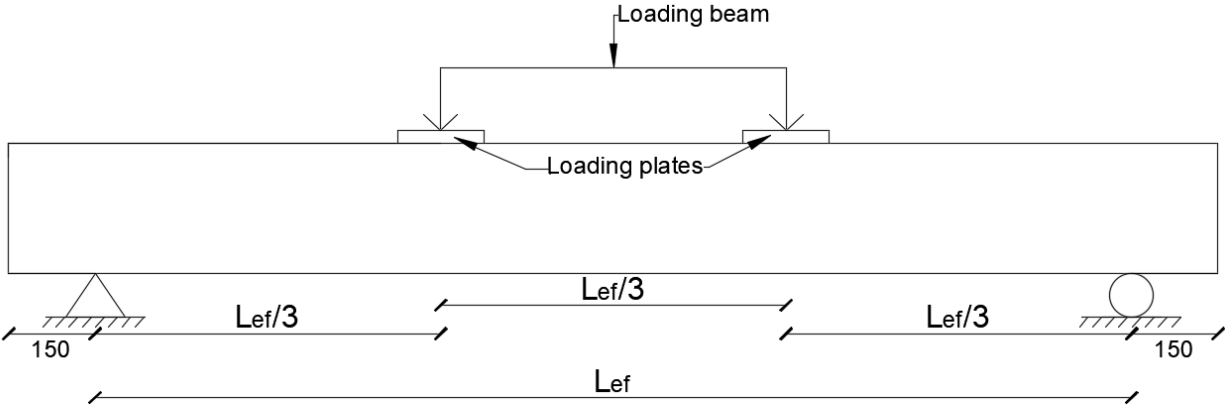


Figure 22: Four-point bending of the corroded RC beam.

## 4. NLFEA of the investigated beams

Modelling of the beams using NLFEA is presented in this Chapter. The modeling procedures of the NLFEA for both Cases A and B are explained in Subchapters 4.1-4.11.

### 4.1 Description of FE-models

The different analyses are described in detail in this Chapter. Case A was split into two subcases as it was modelled with (Subcase A-C) and without the corrosion-induced crack (Subcase A-NC). The corrosion damage on the rebars and the pre-loading crack pattern including all other parameters were the same for both cases. Case B was analyzed with the corrosion-induced crack in addition to the corrosion damages and pre-loading cracks modelled on the beam. The FRP components were added in the following order: FRP plate, inclined U-jackets, and then the vertical U-jackets for Case A and B. However, for Case B the vertical U-jackets were added in two steps starting with five vertical U-jackets near each support followed by the addition of vertical U-jackets along the whole length of the beam, see Table 1.

Table 1: Overview of the cases.

		FEA model	Description
Case A	Subcase A-C (With corrosion-induced crack)	A-C-NF	Non-strengthened beam.
		A-C-P	Strengthened with FRP plate.
		A-C-P-IU	Strengthened with FRP plate and Inclined U-jackets.
		A-C-P-IU-U	Strengthened with all FRP components.
	Subcase A-NC (Without corrosion-induced crack)	A-NC-NF	Non-strengthened beam.
		A-NC-P	Strengthened with FRP plate.
		A-NC-P-IU	Strengthened with FRP plate and Inclined U-jackets.
		A-NC-P-IU-U	Strengthened with all FRP components.
Case B (With corrosion-induced cracks)	B-C-NF	Non-strengthened beam.	
	B-C-P	Strengthened with FRP plate.	
	B-C-P-IU	Strengthened with FRP plate and Inclined U-jackets.	
	B-C-P-IU-SU	Strengthen with all FRP components but Vertical U-jackets only near to the supports	
	B-C-P-IU-U	Strengthened with all FRP components.	

C – Modelled with horizontal corrosion crack

NC – Modelled without any corrosion crack

NF – No FRP strengthening

P – Strengthened with FRP plate

IU - Strengthened with inclined U-jackets

SU – Strengthened with vertical U-jackets near to the supports but not in the mid-span

U - Strengthened with vertical U-jackets

## 4.2 Modelling of RC beams

Structural 3D modelling was used to model the beam geometry as the pre-loading induced cracks and the pits along the beam were asymmetrical. 3D-solid elements were used to model concrete whereas, 3D plane membrane elements were used to model FRP components. Also, the reinforcement provided to the beams were modelled as 1D beam elements. The compression bars along with the stirrups were modelled as embedded reinforcement assuming full interaction to the concrete, whereas the tensile rebars were assigned a bond stress-slip relationship based on the level of corrosion. The interaction between the tensile bars and concrete is explained in Chapter 4.6. Solid elements with steel properties were used to model the support plates and loading plates with a thickness of 25 mm. Structural plane interface elements were used to connect the loading plate and support plate to the concrete surface. The loading beam was modelled 225 mm and 300 mm above the beam for Case A and B respectively. The nodes at the end of the loading beam were tied to the centre lines of the loading plates in the Z direction. Moreover, the horizontal motion of the loading beam in X direction was prevented by restraining it at a node in the centre to maintain stability, see Figure 23-24. The support plates were restrained vertically in Z direction and one of the two support plates was restrained in the X direction.

The complete beam geometry was modelled for Case A and the centre nodes of the support plates were restrained in Y direction as shown in Figure 23. As the beam geometry for Case B was considerably larger, a symmetry line along the beam running through the centre of the cross section was used in order to save computational time. This was carried out by restraining the faces and nodes passing through the symmetry line in Y direction as shown in Figure 24.

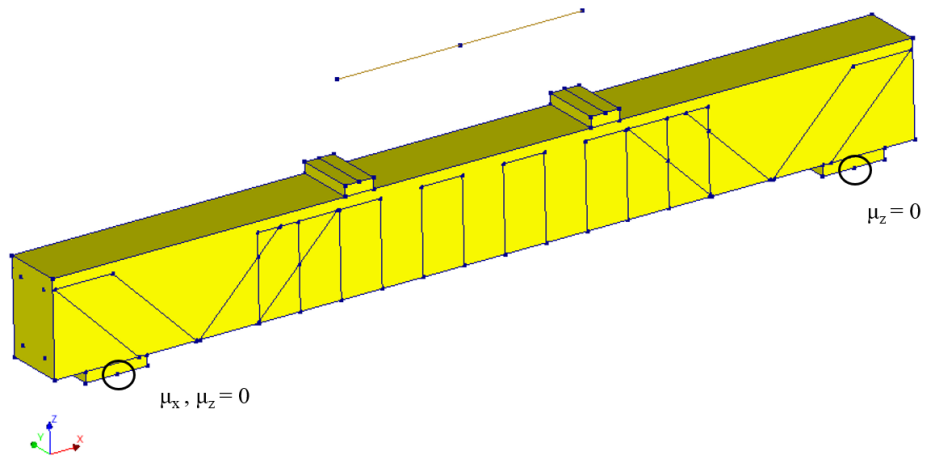


Figure 23: Beam geometry with support conditions modelled for Case A.

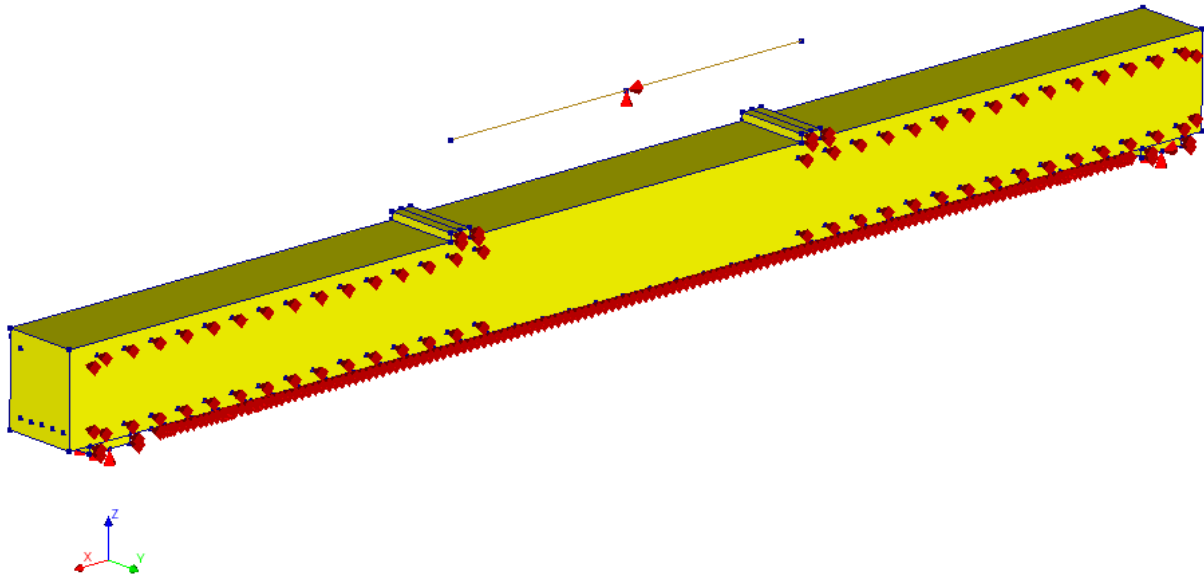


Figure 24: Beam geometry with support conditions and symmetry modelled for Case B.

### 4.3 Material properties for concrete

Compression and wedge split tests have been performed by Yang et al. [8] to determine the material properties of concrete used in the experiment. As it was chosen to keep material properties of concrete to be constant, the same values were used in both cases. The values and equations taken from Yang [8] and from *fib* model 2010 [43], are presented in Table 2. A smeared crack approach together with a rotating crack model was chosen to model cracking in the analyses. The crack band width was calculated as  $\sqrt[3]{V}$ , where  $V$  is the volume of 3D concrete element according to Rots [44]. The effect of lateral cracking was taken into consideration and a reduction factor of 0.6 was used according to [45], which was the lower bound value.

Table 2: Concrete properties.

Concrete properties		Value
Mean compressive strength [8], [43]	$f_{cm} = 0.8f_{cm.cube}$	63 [MPa]
Mean tensile strength [43]	$f_{ctm} = 2.12\ln(1 + 0.1f_{cm})$	4.21 [MPa]
Tensile fracture energy [8]	$G_f$	134 [N/m]
Compression fracture energy [43]	$G_c = 250G_f$	33500 [N/m]
Young modulus [8]	$E_{cm}$	33.3 [GPa]

Both tensile and compressive curves for the concrete were estimated based on the respective fracture energy. The tensile curve for concrete given by Hordijk [46] is shown in Figure 25(a). The compressive curve was presented by Feenstra [47] as illustrated in Figure 25(b).

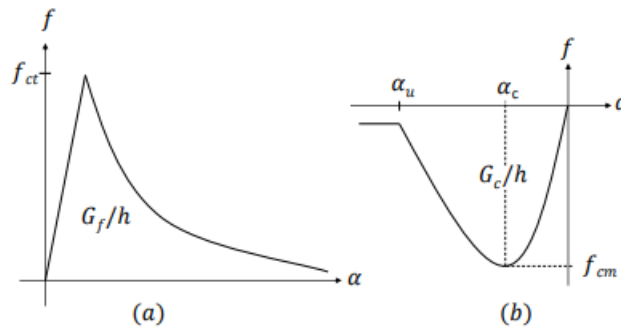


Figure 25: (a) The tensile curve by Hordijk (b) The parabolic compression curve by Feenstra. [12] with permission.

## 4.4 Material properties for steel

To assign material properties for the reinforcement bars, the tensile stress-strain relationship as shown in Figure 26 was used as input for the FE analysis. Standard tensile tests were carried out by Yang [8] and the test results have been used to obtain the stress-strain properties for steel reinforcement. Six tensile tests were conducted for both the top and bottom rebars and a suitable fitting curve corresponding to the average results from the tests by Franklin and Gotame [12] was chosen as the input for the NLFEA. The reinforcement properties for the tensile and compressive bars along with the stirrups are presented in Appendix A.

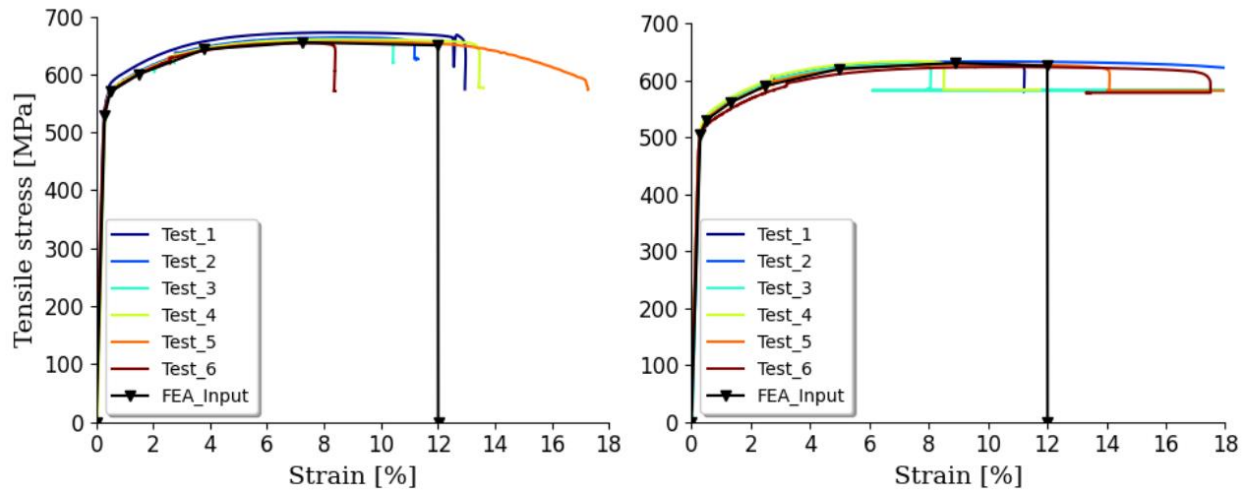


Figure 26: Tensile stress-strain relationship for tensile bars (left) and compressive bars (right) [12], with permission.

## 4.5 Loading and support plates

Steel loading and support plates were used at the location of loading and support points. The plates were used to prevent stress concentration at the position of loading. Linear steel properties were assigned to the steel plates with an Elastic modulus of 200 GPa and Poisson's ratio of 0.3. Interface properties between loading/supports plates, and concrete were assumed according to Belletti [48], as shown in Table 3. Where, DSNX and DSNY are the shear moduli in the direction of X and Y axes respectively, and DSNZ is the normal stiffness modulus in the direction of Z axis.

Table 3: Interface properties between steel plates and concrete.

DSNX	DSNY	DSNZ
$3.42 \cdot 10^5$	$3.42 \cdot 10^5$	$3.42 \cdot 10^{13}$

## 4.6 Interaction between concrete and reinforcement

The interaction between concrete and corroded reinforcement was modelled according to the ARC- model [42]. The effect of corrosion level was considered, and corresponding bond stress-slip relationship was obtained from the ARC-model and applied into modelling. Material data for rebars and concrete, rebar geometry and corrosion level were input to the ARC model. Furthermore, a good bond condition was assumed. The inputs for Case A and Case B were different which led to different bond stress-slip relationships, as shown in Figure 27 and 28. It can be noted that the corrosion level was large enough such that only the residual branch in the bond stress-slip relationship remained.

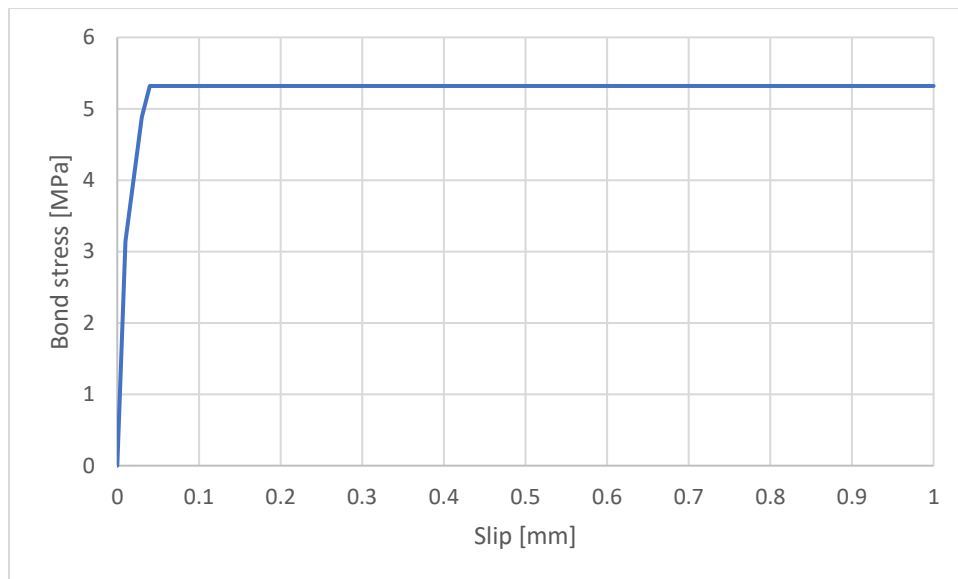


Figure 27: Bond stress-slip relationship for Case A.

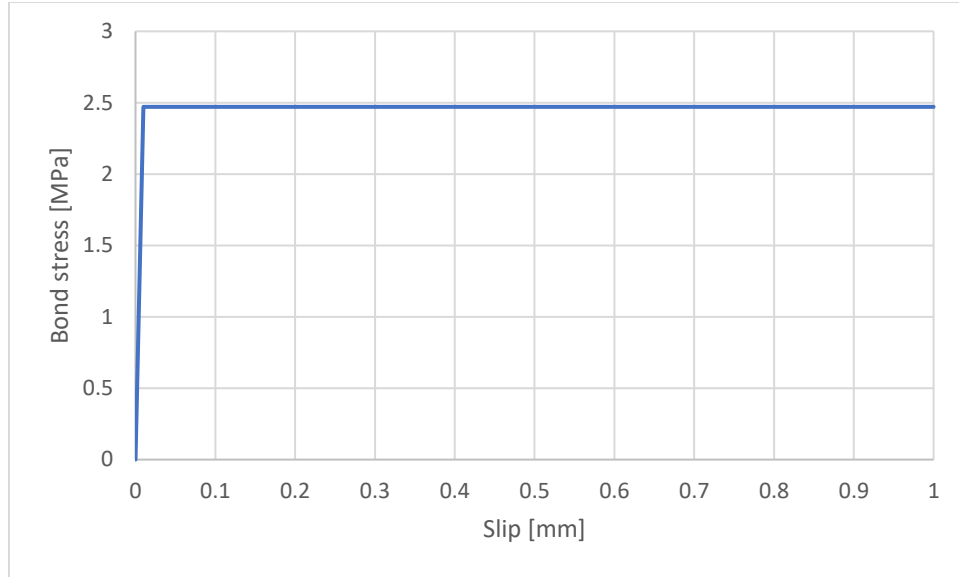


Figure 28: Bond stress-slip relationship for Case B.

In order to implement the bond stress-slip relationship into NLFEA, a multilinear bond-slip curve was chosen as an interface failure model. The initial normal stiffness modulus was set to  $10^{12}$  N/m<sup>3</sup> and the shear stiffness modulus was set to  $10^{11}$  N/m<sup>3</sup>. The compressive rebars and the stirrups were modelled with full interaction.

## 4.7 FE mesh

The concrete was modelled in the NLFEA as 3D solid continuum elements: Pyramid (PY15L), tetrahedrons (TE12L), bricks (HX24L), and wedges (TP18L). Linear interpolation and gauss integration was implemented into all element types. The size of the mesh was chosen to be 20 mm by taking lower value of  $(\frac{l}{50}, \frac{h}{6}, \frac{b}{6})$ , according to Hendriks [49]. The mesh size for the FRP plate was chosen to be 5 mm, as per the recommendation by Kalfat [50]. The interface elements between all components were modelled using element type Q24IF. The element type for the loading beam was chosen as three-dimensional beam elements with two nodes (L12BEA). Beam elements was chosen to model reinforcement bars. The 3D model from NLFEA of the meshed beam in Case B is illustrated in Figure 29

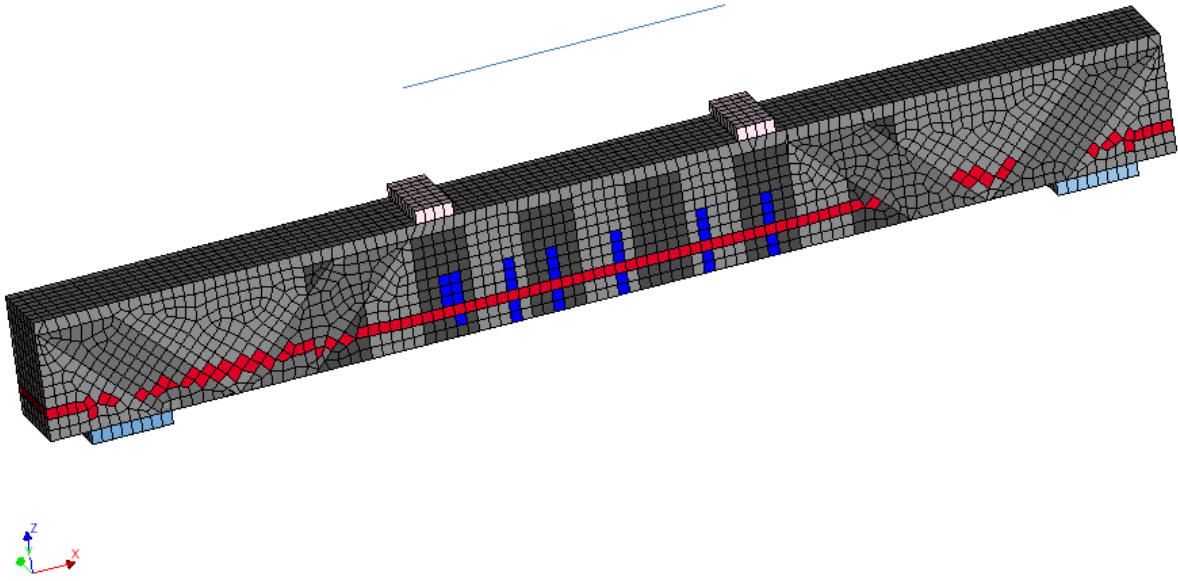


Figure 29: The meshed beam from Case A.

## 4.8 Modelling of pre-loading cracks

A smeared crack approach was used to model the pre-loading and corrosion-induced cracks into the model. The cracks were smeared over the concrete elements at the location of cracks by weakening the corresponding concrete elements by reducing the tensile strength according to Blomfors et. al. [51], [52]. The crack widths for longitudinal and pre-loading cracks were assumed to be constant along the entire crack length and width of the beam respectively.

A bilinear stress to crack opening relationship [53] as shown in Figure 30 was used to calculate the reduction of tensile properties for concrete elements at the cracks using Equation 5.2.

$$\sigma_s = 0.25 \cdot f_{ctm} \quad w_{ult} = \frac{5 \cdot G_f}{f_{ctm}} \quad w_s = 0.15 \cdot w_{ult} \quad (5.2)$$

For Case A, the crack widths were extracted from the experiment by Yang [8], whereas for Case B the crack widths for all the pre-loading cracks were assumed to be constant and calculated based on the mean crack spacing for a service load which is presented in Appendix E. The crack width for corrosion-induced cracks in Case B was assumed to be the same as for Case A.

From Figure 30 (a) for bilinear mode-I stress-crack opening relationship, the tensile stress ( $f_{ct,c}$ ), and fracture energy ( $G_{F,wc}$ ), for the different crack widths were obtained. For crack widths larger than ( $w_{ult}$ ), the tensile strength was calculated with respect to ( $0.99 \cdot w_{ult}$ ) to avoid having zero tensile strength which would have caused numerical issues.

The crack band width was chosen to be equal to the element size of 20 mm as the cracks were assumed to localize over a single row of elements. The stress-strain relationship is derived from the corresponding stress-crack opening relationship using the assumed crack band width ( $h$ ) and modulus of elasticity ( $E_{cm}$ ) as shown in Figure 30 (b) The resulting stress-strain relationship used for the weakened concrete elements is shown in Figure 30 (c).

$$\epsilon_{wc,ult} = \frac{w_{ult} - w_c}{h} \quad \text{when } w_c > w_s \quad (5.3)$$

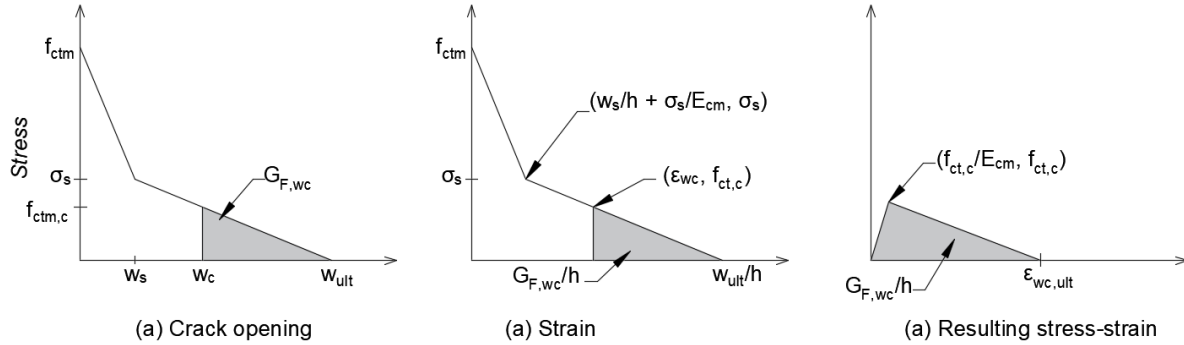


Figure 30: Deriving stress-strain properties for weakened concrete elements, redrawn from Blomfors et. al. [51].

Figures 31 and 32 show 3D representations of how the cracks were modelled in Case A and B respectively. The horizontal corrosion-induced crack was assumed to extend along entire length of the beam. The pre-loading cracks for Case A were modelled based on the experiment by Yang [8]. For Case B, the pre-loading cracks were assumed to extend until the level of the neutral axis.

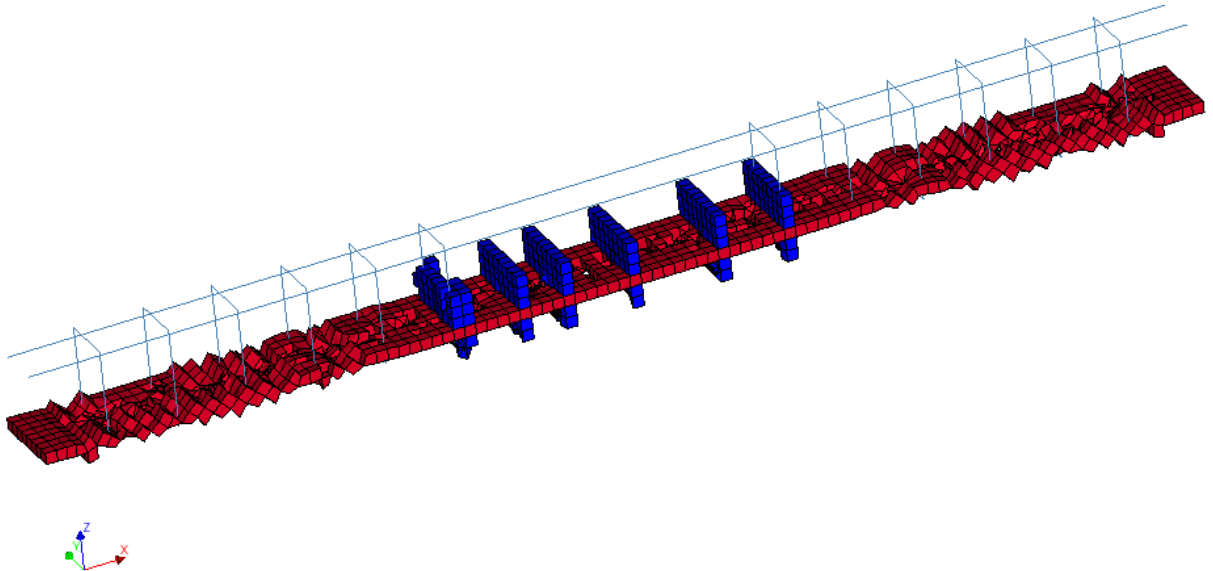


Figure 31: Modelling of cracks for Case A.

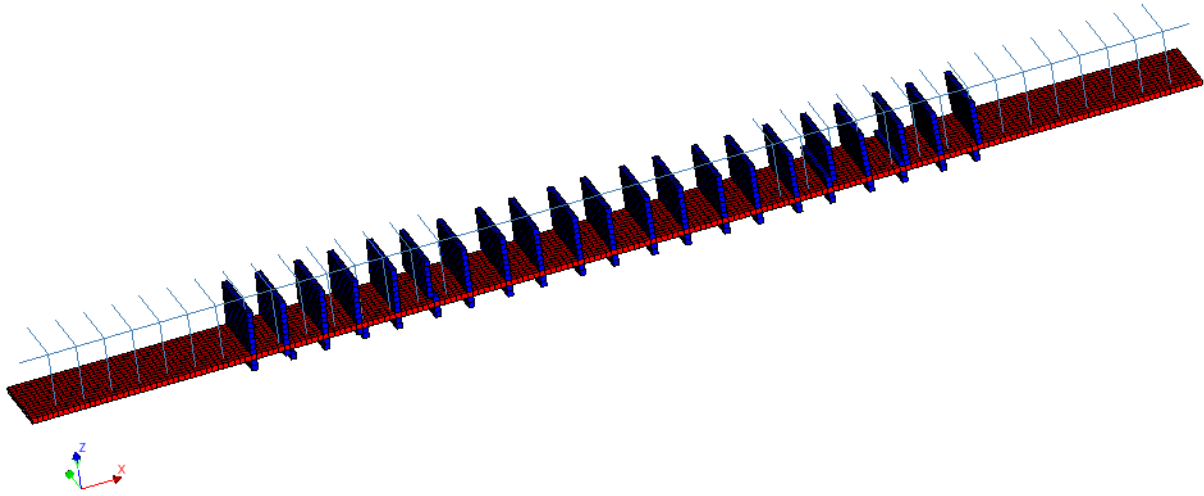


Figure 32: Modelling of cracks for Case B

## 4.9 Modelling of corroded reinforcement bars

The tensile bars were modelled with corrosion level of 20 % indicating that the bars had 80 % of the uncorroded rebar area remaining. The corroded tensile reinforcement was modelled as separate beam elements at the location of the pits, dividing the rebar into pits and general corroded rebars. The area of the reinforcement was reduced based on the level of corrosion as presented in Appendix C. The pits in Case A have different levels of corrosion reflecting that different cross-sectional area is applied on the corresponding pits. The length of the pits were assumed the same as documented in the experiment by assuming the same procedure as Franklin and Gotame [12]. All the pits in Case B were modelled the same with 52% cross sectional area of the uncorroded rebar area. The compression bars and the stirrups were modelled without any reduction in rebar area as they were assumed to be uncorroded.

## 4.10 Modelling of FRP strengthening

The arrangement of FRP components was the same for Case A and B, as explained in Chapter 3.2. The FRP sheets were modelled with quadrilateral 3D plane membrane elements (Q12GME). Two different materials were assigned to FRP sheets: Isotropic or orthotropic material. An isotropic material was assigned to FRP plate and inclined U-jackets, while orthotropic material was assigned to the vertical U-jackets. The properties and dimensions of the FRP components are presented in Table 4. Linear elastic material property was used for FRP sheets which imply a linear stress-strain relationship. Brittle failure occurs when the tensile strength of FRP is reached where the tensile strength is calculated as the product of FRP Elastic modulus ( $E_f$ ) and rupture strain ( $\epsilon_f$ ), see Figure 33(a). The stress-strain relationship for FRP components is presented in Appendix D.

Table 4: The properties and dimensions of FRP components.

FRP Components	Width × Thickness [mm]		$E_{fx}$ [GPa]	$E_{fy}$ [GPa]	$\epsilon_{fu}$ [%]	Y [-]	$G_{xy}$ [GPa]
	Case A	Case B					
FRP plate	100×1.45	450×1.45	214	214	1.27	0.2	-
Inclined FRP	100×2.39		57.6	57.6	1.24	0.2	-
Vertical U-jacket	100×2.39		7.1	57.6	1.24	0.2	5

The element type of the interface elements between concrete and FRP was chosen to be 3D structural plane interface (Q24IF). Bi-linear stress-slip relationship was used to express the non-linear interface properties between FRP and concrete. This method is presented by Lu et al. [54], and based on the following Equations:

$$\begin{aligned} \tau &= \tau_{max}s/s_0 \quad \text{if } s \leq s_0 \\ \tau &= \tau_{max}(s_f - \frac{s}{s_f} - s_0) \quad \text{if } s_0 < s \leq s_f \\ \tau &= 0 \quad \text{if } s > s_f \end{aligned} \quad (5.4)$$

Where,  $s_f = 0.182$  mm,  $s_0 = 0.07$  mm,  $\tau_{max} = 5.74$  MPa, according to Lu et al. [54], see Figure 33(b). The bond stress-slip relationship between FRP/concrete and FRP/FRP were assumed to be the same, see Appendix D. This assumption was made as there was no information found regarding interface properties between FRP/FRP in the existing literature.

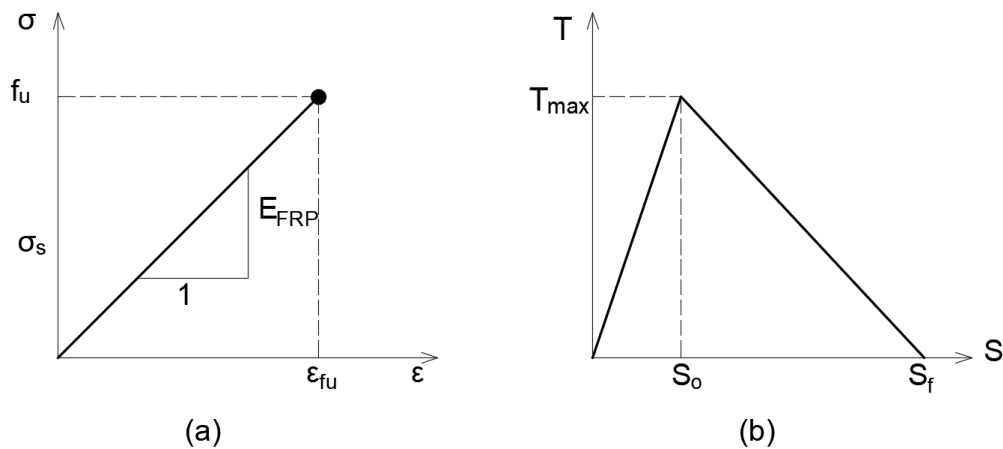


Figure 33: (a) Stress-strain relationship for FRP components, (b) Bond stress-slip for the interface between concrete and FRP. From [12], with permission.

## 4.11 Load steps and convergence criteria

The analyzed beams were subjected to four-point bending as shown in Figure 22. The deformation-controlled load was applied in different steps for the two different cases. For Case A, the loading was applied in 250 steps of 0.02 mm deformation and thereafter by 500 steps of 0.05 mm deformation. For Case B, the loading was applied in 500 steps of 0.05 mm followed by 400 steps of 0.1 mm. The iteration method was chosen to be Secant (Quasi-Newton) where the secant method 'BFGS' (Broyden, Fletcher, Goldfarb, and Shanno) was selected. The maximum number of iterations was set to a value of a 400 as chosen by Franklin and Gotame [12]. The energy norm and the force norm were chosen to be 0.0001 and 0.01, respectively, as tolerance limits for convergence.

## 5. Results of NLFEA

The results from the NLFEA of both the cases A and B are presented in this Chapter. The flexural behaviour of the cases and subcases in Chapter 4.1 are investigated and discussed. Initially, the failure modes were investigated, and the resulting load-deflection graph is presented for all the subcases. The change in failure mode and the effect of strengthening is studied by plotting the load-deflection graphs when the FRP plate, inclined U-jackets and vertical U-jackets were added.

### 5.1 Subcase A-C with corrosion-induced crack

The failure modes for Case A with different FRP configurations which was modelled with the corrosion induced cracks is presented in Table 5. The load-deflection graph for all the subcases provides an overview of the effect of adding individual FRP components in steps, see Figure 34.

Table 5: Failure modes for Subcase A-C, with corresponding load and deflection at failure.

FEA model	Total failure load [kN]	Mid-span deflection [mm]	Failure mode
A-C-NF	43.6	10.3	Rebar rupture
A-C-P 	74.2	6.3	Local concrete cracking at the edge of FRP plate
	77.5	10.5	Shear crack delamination
A-C-P-IU 	120.0	10.2	Interfacial delamination
A-C-P-IU-U 	121.1	9.7	Interfacial delamination

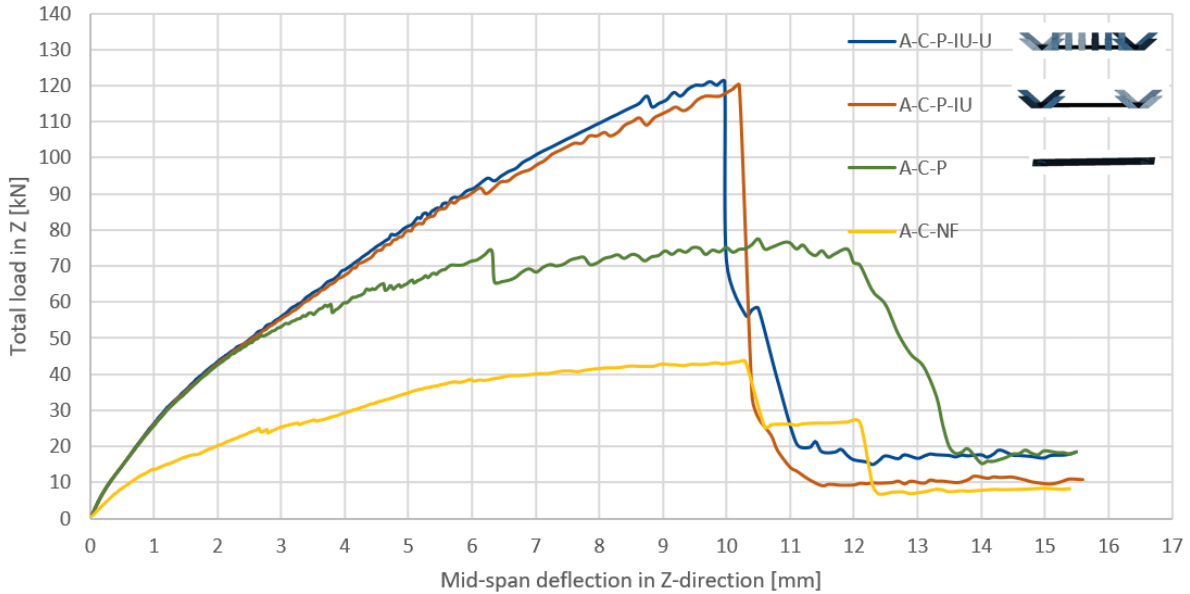


Figure 34: Overview of load versus mid-span deflection graphs for Subcase A-C.

### 5.1.1 Non-strengthened beam (A-C-NF)

The failure mode from the analysis of A-C-NF was rebar rupture; the rebars failed at the pits. The failure occurred when the strain in the rebars exceeded the ultimate strain value of 0.12. Rupture of tensile bar II at pit IIa was observed as shown in Figure 35(b) followed by the rupture of tensile bar I at pit Ia, see Figure 35(c).

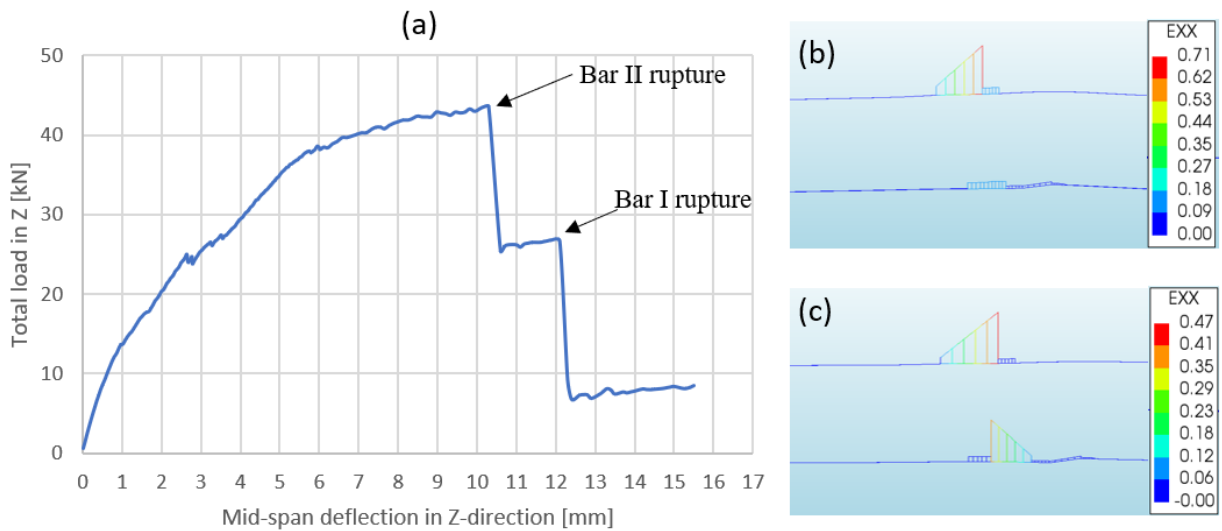


Figure 35: (a) Load versus mid-span deflection graph for FEA model A-C-NF, (b) Strain diagram showing bar II rupture at mid-span deflection of 10.5 mm, (c) Strain diagram showing bar I rupture at failure at mid-span deflection of 12.5 mm.

## 5.1.2 Beam strengthened with FRP plate (A-C-P)

The failure mode from the analysis of A-C-P began with local concrete cracking at the edge of the FRP plate, followed by shear crack delamination as shown in Figure 36. In order to investigate the failure mode, the relative displacement between a set of two points at the centre and at the edge was plotted. One point was selected at the beam soffit and the other point was selected at a distance (twice the element size) above the horizontal corrosion crack, see Figure 37.

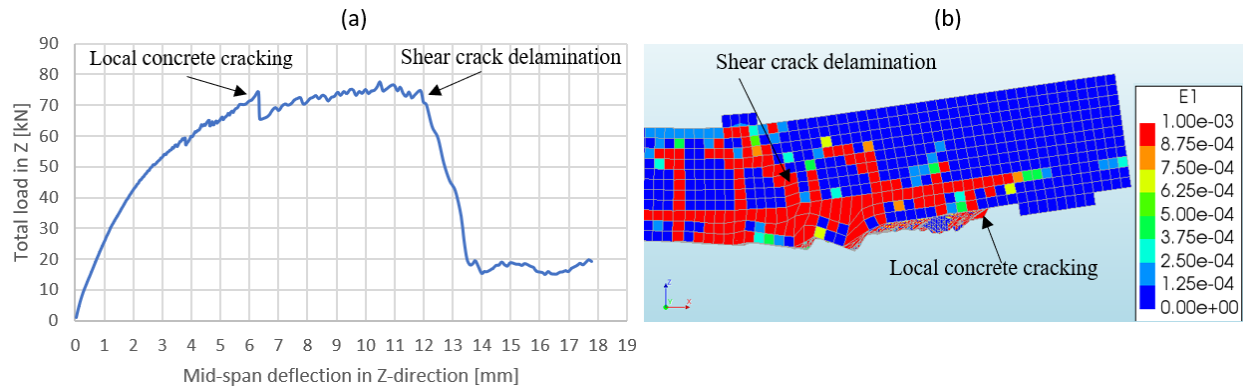


Figure 36: (a) Load versus mid-span deflection graph for FEA model A-C-P. (b) Principal strain showing the resulting failure modes at mid-span deflection of 12.5 mm.

To investigate the first drop in the load-deflection graph, two sets of points were selected, with one set at the edge of the beam and the other at the centre of the beam, see Figure 37 (b). In Figure 37 (a) the crack opening at the edge and the centre points is plotted with the load versus mid-span deflection. This graph shows that the crack opened more at the centre of the beam, indicating that there was local concrete cracking near the FRP plate edge.

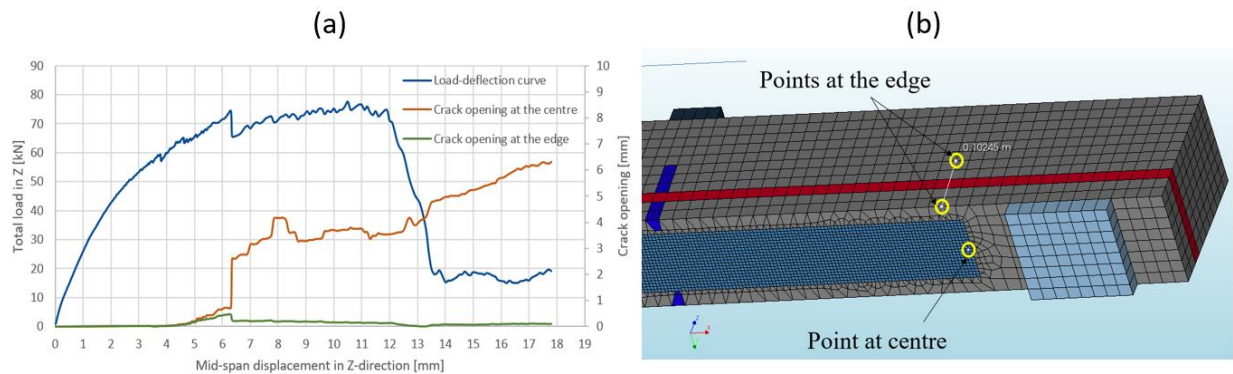


Figure 37: (a) Load and crack opening versus relative displacement graph for FEA model A-C-P. (b) Sets of point selected for failure mode investigation.

To investigate the second drop in the load-deflection curve, a single set of points was selected as highlighted in Figure 38 (b), and the load and crack opening vs mid-span deflection was plotted as shown in Figure 38 (a). An increase in the crack opening was observed from the first failure until the final failure. This indicates that the beam failed due to shear crack delamination as there was delamination of concrete at the position of the chosen set of points.

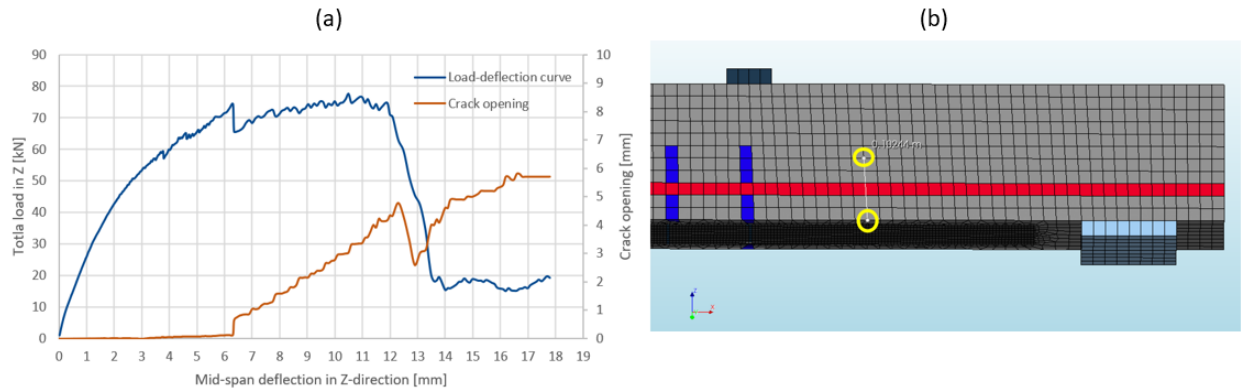


Figure 38: (a) Load and crack opening versus mid-span deflection graph for the set of points. (b) The set of points selected for failure mode investigation.

### 5.1.3 Beam strengthened with FRP plate and inclined U-jackets (A-C-P-IU)

The failure mode from analysis of A-C-P-IU was observed to be interfacial delamination of FRP plate near the plate end. The load-deflection curve for this case is shown in Figure 39 (a). The investigation of failure mode was done by looking at the relative interface displacement (DUSx), see Figure 39 (b). A sudden increase in the (DUSx) was observed at the load step where there was a sudden drop in the load-deflection curve.

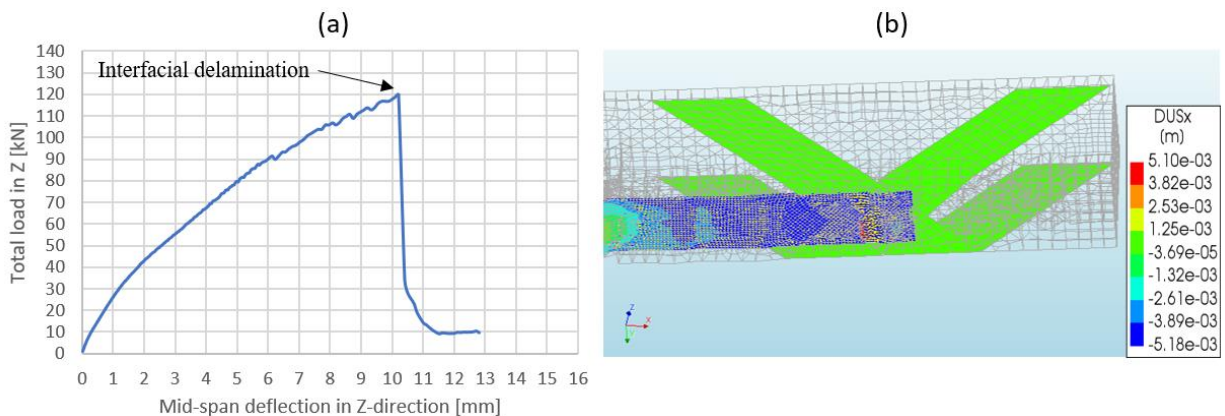


Figure 39: (a) Load versus mid-span deflection graph for FEA model A-C-IU. (b) Relative interface displacement between FRP and concrete at mid-span deflection of 10.5 mm.

### 5.1.4 Beam strengthened with all FRP components (A-C-P-IU-U)

The failure mode from the analysis of A-C-IU-U was interfacial delamination of the FRP plate near the plate end similar to the results of the analysis of A-C-P-IU. The investigation was carried out by checking the relative interface displacement as shown in Figure 40 (b). The resulting load-deflection curve is shown in Figure 40 (a).

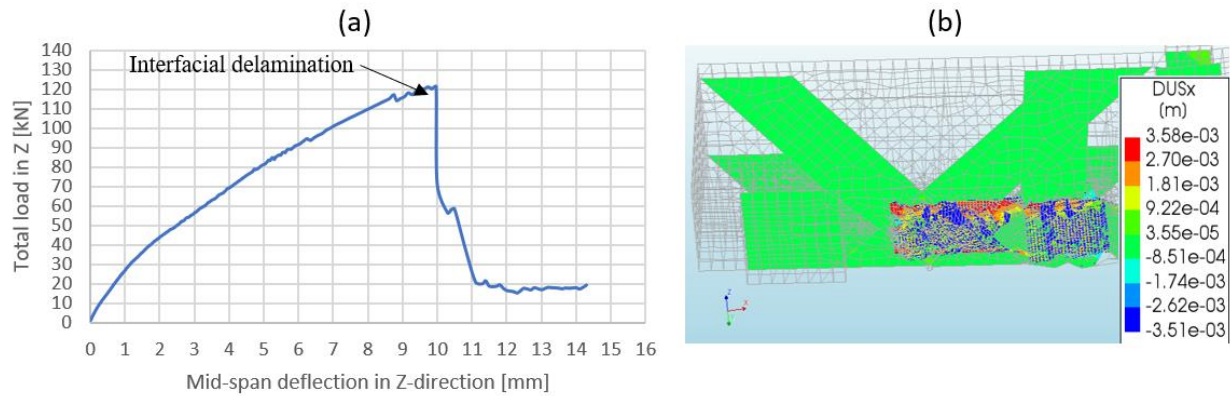


Figure 40: (a) Load versus mid-span deflection graph for FEA model A-C-P-IU-U. (b) Relative interface displacement between FRP and concrete at the mid-span deflection of 10.2 mm.

## 5.2 Subcase A-NC without corrosion-induced crack

As Case A was modelled with and without corrosion induced cracks, a comparison of the load-deflection curves along with the failure modes is shown in Figure 41 for each subcase. The ultimate load-bearing capacity and the corresponding deflection of the beams were nearly the same. However, small difference in deformation capacity was observed for the non-strengthened beams (A-C-NF and A-NC-NF) and different flexural response was observed for the beams strengthened with just the FRP plate (A-C-P and A-NC-P).

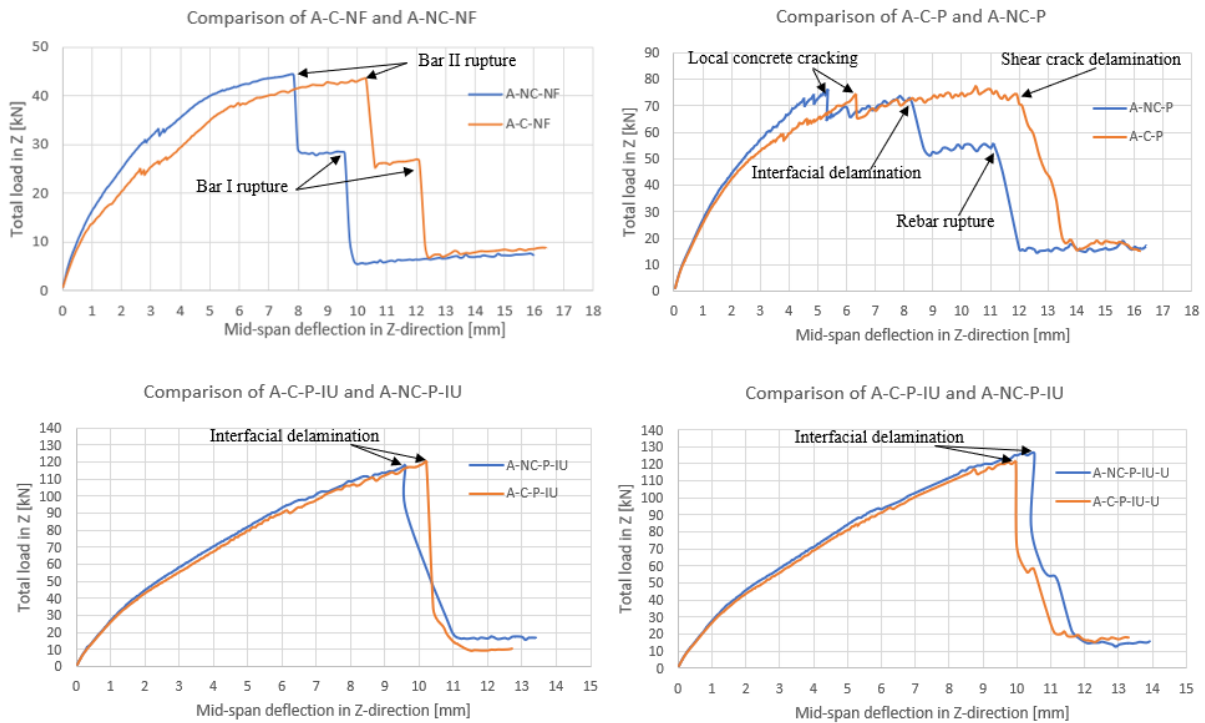


Figure 41: Comparison of Load versus mid-span deflection curves with failure modes for Case A with and without corrosion cracks.

The comparison of failure modes for the analysis of A-NC-P and A-C-P showed that the horizontal corrosion-induced crack resulted in the change of failure mode from interfacial delamination to shear crack delamination. Figure 42 (b) shows the relative interface displacement at the second drop showing that the beam from the analysis of A-NC-P fails due to interfacial delamination.

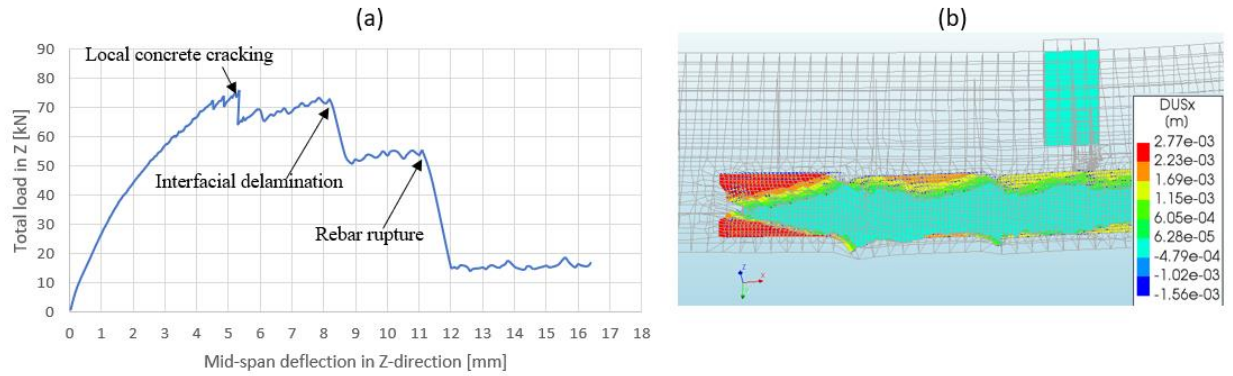


Figure 42: (a) Load versus mid-span deflection graph for FEA model A-NC-P. (b) Relative interface displacement between FRP and concrete at the mid-span deflection of 8.5 mm.

### 5.3 Case B

The results from the investigation for Case B is presented in this chapter. As the beam for Case B was modelled with a symmetry line running along the center of the cross section, twice the loads obtained from the analyses is taken to consider the complete beam geometry. The main results are given in Table 6. Some of the cases have several drops in the load-deflection graph, caused by subsequent failure modes. Therefore, the corresponding load and deflection for those drops are also presented for those cases. A comparison of load-deflection graphs between the subcases of Case B is illustrated in Figure 43.

Table 6: Failure modes for Case B, with corresponding load and deflection at failure.

FEA model	Total failure load [kN]	Mid-span deflection [mm]	Failure mode
B-C-NF	179	64.4	Rebar rupture
B-C-P 	272	22	Concrete cover separation
	266	24.4	Shear crack delamination
B-C-P-IU 	286	25.3	Shear crack delamination
B-C-P-IU-SU 	338	28.7	Shear crack delamination
B-C-P-IU-U 	328	27.7	Shear crack delamination

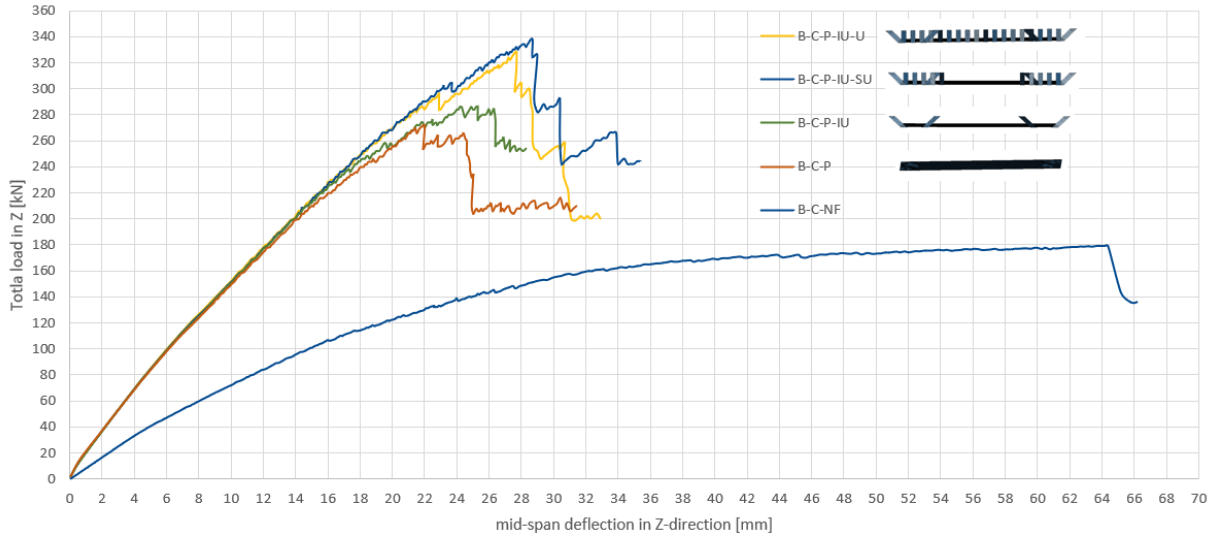


Figure 43: Load versus mid-span deflection graphs for Case B.

### 5.3.1 Non-strengthened beam (B-C-NF)

The failure mode for FEA model B-C-NF was rebar rupture where the rebars failed at the pits. The failure occurred when the strain in the rebars exceeded the ultimate strain value of 0.12. Load-deflection graph is shown in Figure 44 (a) which shows a drop at the failure of bar II. The investigation was carried out by checking the reinforcement strain, see Figure 44 (b). On further loading, similar drops in the load-deflection curve are expected as result of the failure of remaining rebars.

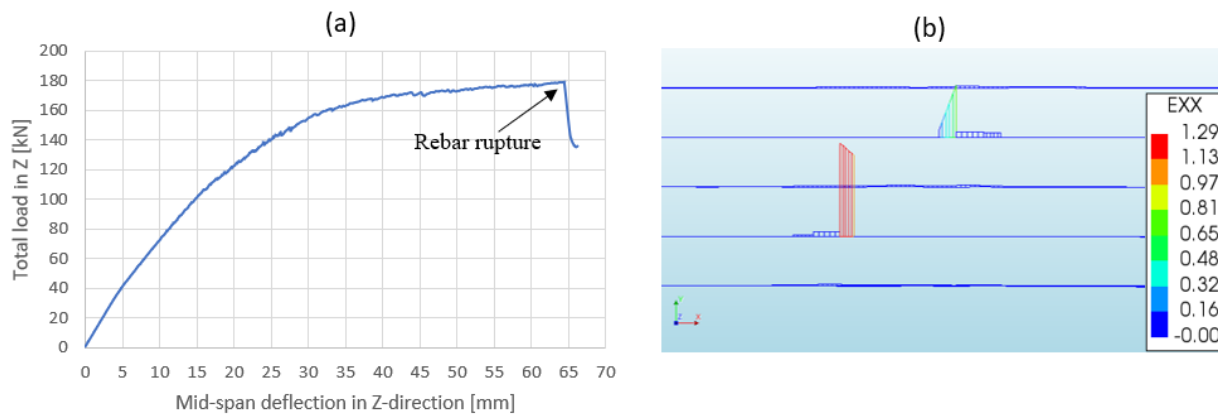


Figure 44: (a) Load versus mid-span deflection graph for FEA model B-C-NF, (b) Strain diagram showing bar II rupture at the mid-span deflection of 65 mm.

### 5.3.2 Beam strengthened with FRP plate (B-C-P)

The failure mode from the analysis of B-C-P started with concrete cover separation at the edge of the FRP plate followed by shear crack delamination as shown in Figure 45.

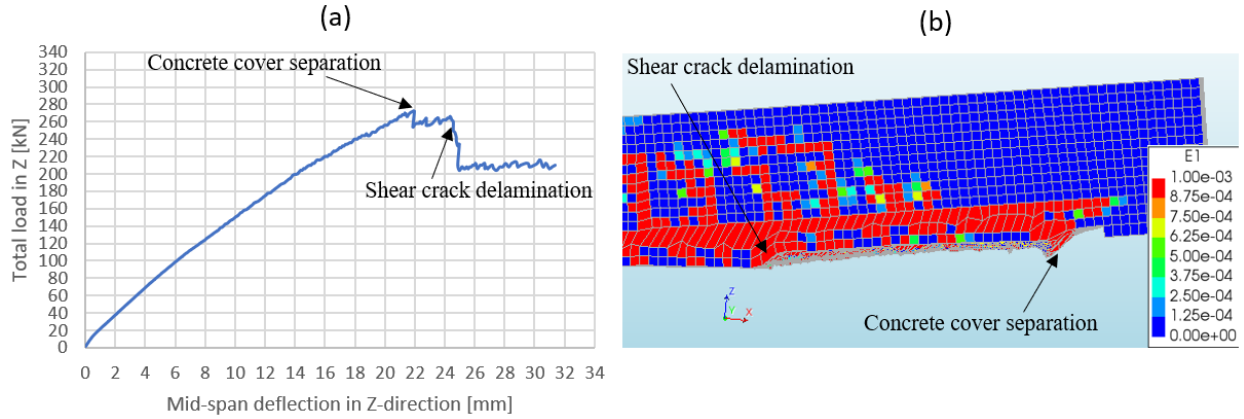


Figure 45: (a) Load versus mid-span deflection for FEA model B-C-P. (b) Principal strain showing the resulting failure modes at the deflection of 25 mm.

The first drop in the load-deflection curve could be explained because of concrete cover separation near the plate end. The second drop could be explained because of the appearance of shear crack that propagated and reached the concrete surface at the beam soffit. The investigation for concrete cover separation was carried out by following the same procedure as for the analysis A-C-P and the crack opening was plotted for the sets of points as shown in Figure 46 (a). As the crack opening was almost the same for both sets of points, it showed that the concrete elements cracked similarly at the edge and at the centre proving it was concrete cover separation and not local concrete cracking.

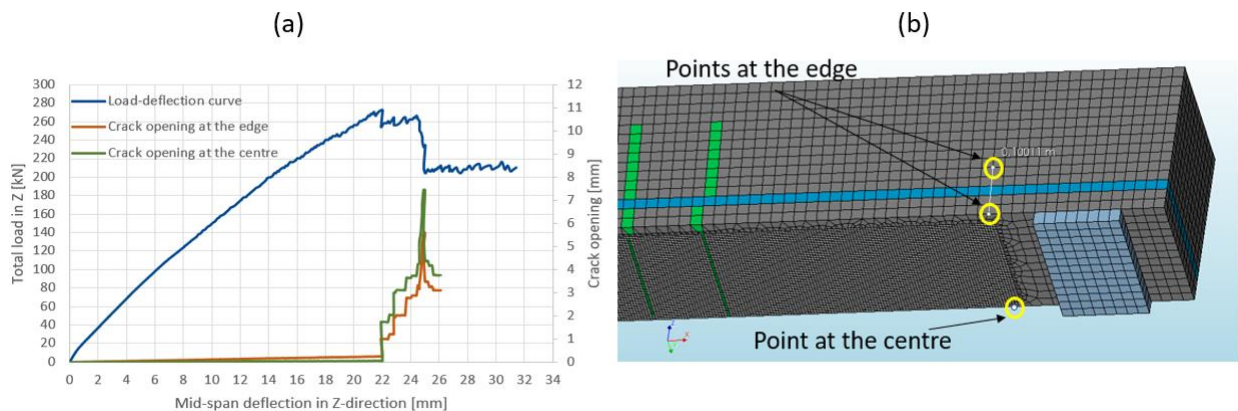


Figure 46: (a) Load and crack opening versus mid-span deflection graph for FEA model B-C-P-IU. (b) Sets of point selected for failure mode investigation.

### 5.3.3 Beam strengthened with FRP plate and inclined U-jackets (B-C-P-IU)

The failure mode from the analysis of B-C-P-IU was observed to be shear crack delamination, as shown in Figure 47. The crack started to grow from the edge of the inclined U-jacket until it reached the concrete surface on the beam soffit causing failure.

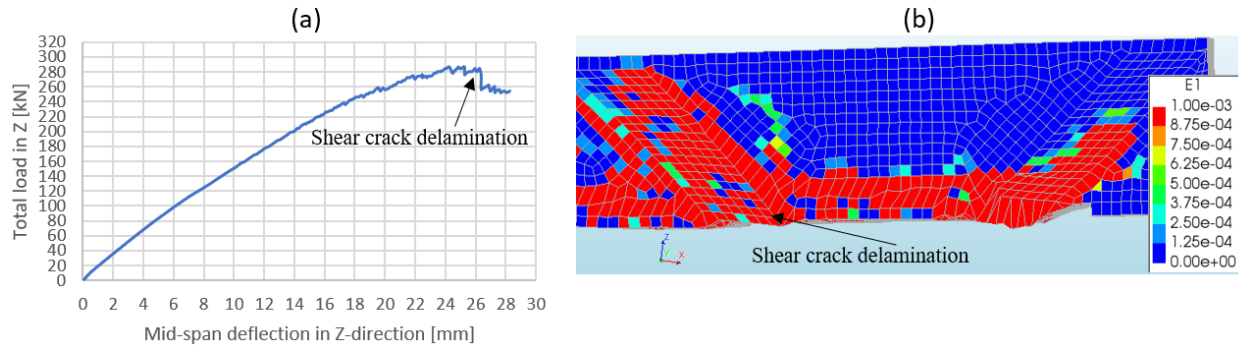


Figure 47: (a) Load versus mid-span deflection for FEA model B-C-P-IU. (b) Principal strain showing the resulting failure at the mid-span deflection of 26.5 mm.

### 5.3.4 Beam strengthened with all FRP components with vertical U-jackets only near the supports (B-C-P-IU-SU)

The failure mode from the analysis of B-C-P-IU-SU was found to be shear crack delamination. The vertical U-jackets close to the supports cause a change in the position of shear crack shifting it closer to the support compared to the analysis of B-C-P-IU, see Figure 48.

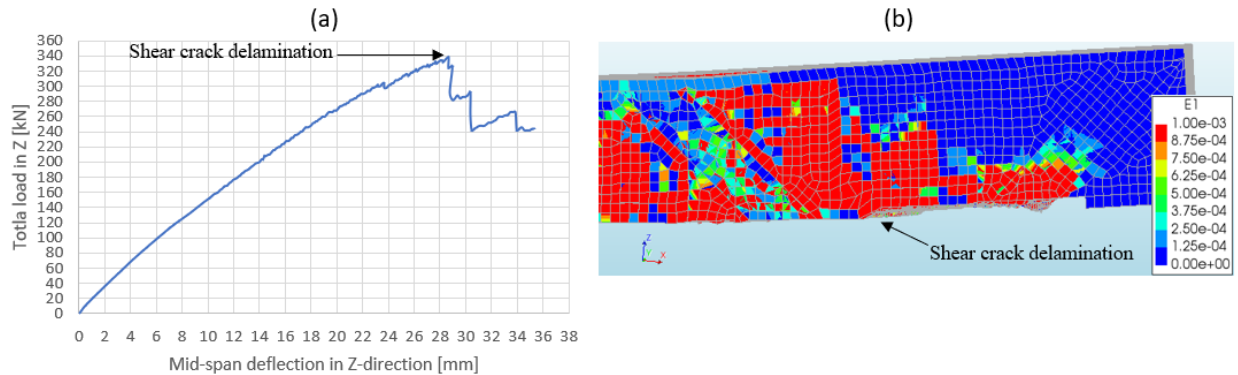


Figure 48: (a) Load versus mid-span deflection for FEA model B-C-P-IU-SU. (b) Principal strain showing the resulting failure at the mid-span deflection of 29 mm.

### 5.3.5 Beam strengthened with all FRP components (B-C-P-IU-U)

The failure mode from the analysis of B-C-P-IU-U was observed to be shear crack delamination. The load-deflection curve and the corresponding failure mode at the drop is presented in Figure 49.

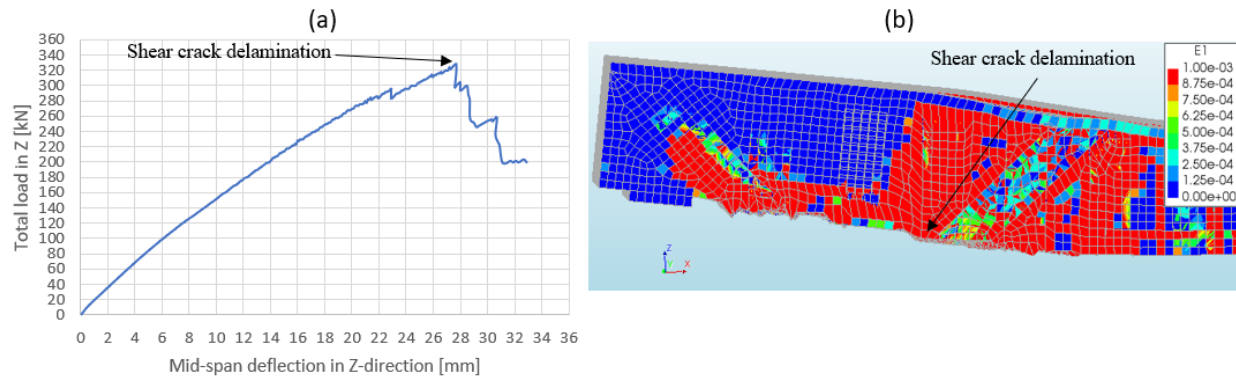


Figure 49: (a) Load versus mid-span deflection for FEA model B-C-P-IU-U. (b) Principal strain showing the resulting failure at mid-span deflection of 28 mm.

## 6. Discussions

The flexural behaviour and failure modes of the beams with corroded reinforcement was studied for two different beam geometries (Case A and Case B) with several variations of the strengthening system. Case A was further divided into two subcases where the corrosion induced crack was modelled in Subcase A-C and excluded in the modelling of Subcase A-NC. For Case B, the beam was designed to have greater width than height and minimum rebar spacing. The cases were strengthened by adding FRP components in steps and the increase in load-bearing capacity was compared to the non-strengthened beam.

For Subcase A-C, when the beam was strengthened with just the FRP plate (A-C-P), the ultimate load-bearing capacity increased by 78%. Two drops were observed in the load-deflection graph caused by local concrete cracking and shear crack delamination. Local concrete cracking was the first failure that occurred at the edge of the FRP plate, and shear crack delamination was the second failure observed near the loading plate at the beam soffit. To investigate the effectiveness of FRP on different beam geometry, Case B was analyzed. When the beam was strengthened with FRP plate (B-C-P), two drops in the load-deflection graph was observed which were due to concrete cover separation at the edge of the FRP plate followed by shear crack delamination. The ultimate load-bearing capacity was increased by 52% with respect to the non-strengthened beam. The beam with height larger than the width (Case A) showed larger increase in load-bearing capacity than the beam with width larger than the height (Case B).

The inclined U-jackets were added to the beams strengthened with FRP plate as the next step to investigate its effectiveness. As result, for Subcase A-C the ultimate load-bearing capacity increased from 78% to 175% with respect to the non-strengthened beam and the failure was observed to be interfacial delamination of the FRP plate. The inclined U-jackets were able to prevent shear crack delamination and provide better anchorage of the FRP plate. For Case B, the addition of inclined U-jackets caused no significant improvement of the ultimate load-bearing capacity with an increment from 52% to 60% with respect to the non-strengthened beam. Here, concrete cover separation near the plate end was prevented, and the beam failed due to shear crack delamination at the edge of the inclined U-jacket. Thus, the inclined U-jackets were effective in strengthening Case A but not Case B. This could be explained as the chosen inclined U-jacket arrangement, dimension and inclination was suitable for the geometry of Case A but not for geometry of Case B. However, the addition of inclined U-jackets prevented failure at the end of the FRP plate for both cases.

The addition of vertical U-jackets along with other FRP components was the final step of strengthening. For Case B, the addition of vertical U-jackets was split into two steps where the vertical U-jackets were added near the supports (B-P-IU-SU) followed by the addition of vertical U-jackets in the mid-span (B-P-IU-U). Although, for Subcase A-C, the vertical U-jackets were added in a single step in the mid-span region only. For Case A, the vertical U-jackets proved to have negligible effect on the flexural behaviour, causing the beam to fail due to interfacial delamination of FRP plate. The vertical U-jackets did not contribute to prevent the failure due to interfacial delamination near the plate end as they were applied in the mid-span region of the beam.

For Case B with vertical U-jackets near the supports (B-C-P-IU-SU), the ultimate load-bearing capacity was increased from 60% to 89% compared to the non-strengthened beam. The failure mode was due to shear crack delamination at the edge of the inclined U-jackets. The addition of vertical U-jackets could not prevent the shear crack delamination but were able to increase the load-bearing capacity. As the vertical U-jackets were added at the critical sections where shear crack delamination had occurred, an increase in load-bearing capacity was observed. With the addition of vertical U-jackets along the complete length of the beam (B-C-P-IU-U), the increase in the ultimate load-bearing capacity was from 60% to 83% which was lower compared to B-C-P-IU-SU where the vertical U-jackets were added only near the supports. Higher load-bearing capacity was achieved for Case B when the beam was strengthened with vertical U-jackets only near the supports compared to adding them along the full length of the beam resulting in the same failure mode of shear crack delamination. Adding vertical U-jackets in the mid-span, which was not the location of critical section for failure, resulted in negligible increase in load-bearing capacity for Case A and a small decrease in the load-bearing capacity for Case B.

To study the effect of horizontal corrosion-induced crack on the beams, it was excluded from the modelling of Subcase A-NC and the results were compared to the Subcase A-C where the horizontal corrosion-induced crack was modelled. Similar results were observed for all analyses except for the non-strengthened beam and the beam strengthened with the FRP. A small increase in the deformation capacity was observed for the non-strengthened beam when the horizontal corrosion-induced crack was modelled. This could be explained by the behaviour of the beam modelled without horizontal corrosion-induced crack reaching the ultimate load at lower deformation compared to the beam modelled with the horizontal corrosion-induced crack. For the beams strengthened with just the FRP plate, the first failure mode was local concrete cracking for both beams. But the second failure mode was anchorage failure of FRP plate for the beam modelled without horizontal corrosion-induced crack and shear crack delamination for the other beam. The ultimate load for analysis A-NC-P occurred at the first failure, but the ultimate load for analysis A-C-P with horizontal corrosion crack occurred at the second failure. This behaviour could be explained as the beam deflected more reaching higher load after the first failure when the horizontal corrosion-induced crack was excluded from modelling. Hence the presence of horizontal corrosion-induced crack increases the tendency for delamination failure.

The deformation capacities were analysed for both cases and the influence of adding FRP components on deflection at failure was noted. Results for Case A showed no significant influence on the deformation capacities of the beams. Whilst the results for Case B showed that there was a large decrease in the deformation capacities of the beams with the addition of FRP components in comparison to the non-strengthened beam. The non-strengthened beam (B-C-NF) deflected by 64 mm whereas the strengthened beam showed deflections between 22 mm to 29 mm at failure.

## 7. Conclusions and suggestions for further investigations

### 7.1 Conclusion

FE analysis was performed to investigate the effectiveness of FRP strengthening of RC beams with corroded reinforcement. Two geometries were studied: Cases A and B, with height/width/span of 225/150/2100 mm and 300/500/4200 mm respectively. From the results of the analyses of the different cases, the following conclusions were drawn:

- FRP plate added to the beam soffit was effective in increasing the load-bearing capacity for the studied beam geometries.
- The inclined U-jackets increased the load-bearing capacity significantly for Case A, but only to a smaller extent for Case B. The chosen inclination, dimension and arrangement of the inclined U-jackets were thus more effective for the beam geometry for Case A.
- The inclined U-jackets were effective in preventing failure due to concrete cover separation or local concrete cracking near the plate end for both cases.
- Addition of vertical U-jackets were effective when they were placed at the location of critical section where failure was expected. As the failure for both Cases A and B was near the supports when strengthened, the addition of vertical U-jackets in the mid-span was not influential in improving the flexural behaviour.
- Addition of different FRP components caused no significant improvement in the deformation capacities for Case A. For Case B, a drastic decrease in deformation capacity in analyses of strengthened beams compared to non-strengthened was observed.
- The presence of horizontal corrosion-induced crack provokes delamination failure.

## **7.2 Further investigation**

In this Master's Thesis, the main focus was to analyse the effectiveness of FRP strengthening of RC beams with corroded reinforcement. It would be of interest to investigate the effectiveness of this method on other RC elements such as slabs and continuous beams.

As the inclined and vertical U-jackets were not always effective for both Cases A and B, it is of interest to further investigate an effective arrangement of the inclined and vertical U-jackets by changing the inclination, dimension and spacing for different beam geometries. Furthermore, the beams were subjected to four-point bending until failure. Hence, it would be of interest to analyse the behaviour of the beams under different load applications such as distributed load.

## 8. References

- [1] R. Dodge Woodsoon, *Concrete Structures. Protection, Repair and Rehabilitation*. 2009.
- [2] A. Goyal, H. S. Pouya, E. Ganjian, and P. Claisse, “A Review of Corrosion and Protection of Steel in Concrete,” *Arabian Journal for Science and Engineering*, vol. 43, no. 10. Springer Verlag, pp. 5035–5055, Oct. 01, 2018. doi: 10.1007/s13369-018-3303-2.
- [3] I. Fernandez, M. F. Herrador, A. R. Mari, and J. M. Bairán, “Structural effects of steel reinforcement corrosion on statically indeterminate reinforced concrete members,” *Materials and Structures/Materiaux et Constructions*, vol. 49, no. 12, pp. 4959–4973, Dec. 2016, doi: 10.1617/s11527-016-0836-2.
- [4] Y. Zhou, B. Gencturk, K. Willam, and A. Attar, “Carbonation-Induced and Chloride-Induced Corrosion in Reinforced Concrete Structures,” *Journal of Materials in Civil Engineering*, vol. 27, no. 9, p. 04014245, Sep. 2015, doi: 10.1061/(asce)mt.1943-5533.0001209.
- [5] E. Chen, C. G. Berrocal, I. Fernandez, I. Löfgren, and K. Lundgren, “Assessment of the mechanical behaviour of reinforcement bars with localised pitting corrosion by Digital Image Correlation,” *Engineering Structures*, vol. 219, Sep. 2020, doi: 10.1016/j.engstruct.2020.110936.
- [6] B. Täljsten, T. Blanksvärd, and G. Sas, *Kompositförstärkning av betong*. 2016. [Online]. Available: [www.byggstjanst.se](http://www.byggstjanst.se)
- [7] Z. Ahmed, M. M. Asghar, M. N. Malik, and K. Nawaz, “Moving towards a sustainable environment: The dynamic linkage between natural resources, human capital, urbanization, economic growth, and ecological footprint in China,” *Resources Policy*, vol. 67, Aug. 2020, doi: 10.1016/j.resourpol.2020.101677.
- [8] J. Yang, R. Haghani, T. Blanksvärd, and K. Lundgren, “Experimental study of FRP-strengthened concrete beams with corroded reinforcement,” *Construction and Building Materials*, vol. 301, p. 124076, Sep. 2021, doi: 10.1016/j.conbuildmat.2021.124076.
- [9] O. Río, ; C Andrade, ; D Izquierdo, and C. Alonso, “Behavior of Patch-Repaired Concrete Structural Elements under Increasing Static Loads to Flexural Failure”, doi: 10.1061/ASCE0899-1561200517:2168.
- [10] A. H. Al-Saidy and K. S. Al-Jabri, “Effect of damaged concrete cover on the behavior of corroded concrete beams repaired with CFRP sheets,” *Composite Structures*, vol. 93, no. 7, pp. 1775–1786, 2011, doi: 10.1016/j.compstruct.2011.01.011.
- [11] M. Gotame, C. L. Franklin, M. Blomfors, J. Yang, and K. Lundgren, “Finite element analyses of FRP-strengthened concrete beams with corroded reinforcement,” *Engineering Structures*, vol. 257, 2022, doi: 10.1016/j.engstruct.2022.114007.

- [12] C. Lindqvist and F. M. Gotame, “FE Analyses of Strengthened Concrete Beams with Corroded Reinforcement.”
- [13] J. Sim, G. Kim, C. Park, and M. Ju, “Shear strengthening effects with varying types of FRP materials and strengthening methods,” in *American Concrete Institute, ACI Special Publication*, 2005, vol. SP-230.
- [14] “Fire Performance ,” <https://compositesuk.co.uk>, 2022.
- [15] R. Kalfat, R. Al-Mahaidi, and S. T. Smith, “Anchorage Devices Used to Improve the Performance of Reinforced Concrete Beams Retrofitted with FRP Composites: State-of-the-Art Review,” *Journal of Composites for Construction*, vol. 17, no. 1, pp. 14–33, Feb. 2013, doi: 10.1061/(asce)cc.1943-5614.0000276.
- [16] B. Täljsten, “FRP strengthening of concrete structures: new inventions and applications,” *Progress in Structural Engineering and Materials*, vol. 6, no. 3, 2004, doi: 10.1002/pse.174.
- [17] H. Thomsen, E. Spacone, ; Suchart Limkatanyu, and G. Camata, “Failure Mode Analyses of Reinforced Concrete Beams Strengthened in Flexure with Externally Bonded Fiber-Reinforced Polymers”, doi: 10.1061/ASCE1090-026820048:2123.
- [18] H. Pham and R. Al-Mahaidi, “Assessment of available prediction models for the strength of FRP retrofitted RC beams,” *Composite Structures*, vol. 66, no. 1–4, pp. 601–610, Oct. 2004, doi: 10.1016/j.compstruct.2004.05.008.
- [19] E. Y. Sayed-Ahmed, R. Bakay, and N. G. Shrive, “Bond strength of FRP laminates to concrete: State-of-the-art review,” *Electronic Journal of Structural Engineering*, vol. 9, 2009.
- [20] C. Chen, X. Wang, L. Sui, F. Xing, X. Chen, and Y. Zhou, “Influence of FRP thickness and confining effect on flexural performance of HB-strengthened RC beams,” *Composites Part B: Engineering*, vol. 161, pp. 55–67, Mar. 2019, doi: 10.1016/j.compositesb.2018.10.059.
- [21] X. Xue and H. Seki, “Influence of Longitudinal Bar Corrosion on Shear Behavior of RC Beams,” 2010.
- [22] L. Wang, X. Zhang, J. Zhang, Y. Ma, and Y. Liu, “Effects of stirrup and inclined bar corrosion on shear behavior of RC beams,” *Construction and Building Materials*, vol. 98, pp. 537–546, Nov. 2015, doi: 10.1016/j.conbuildmat.2015.07.077.
- [23] C. A. Juarez, B. Guevara, G. Fajardo, and P. Castro-Borges, “Ultimate and nominal shear strength in reinforced concrete beams deteriorated by corrosion,” *Engineering Structures*, vol. 33, no. 12, pp. 3189–3196, Dec. 2011, doi: 10.1016/j.engstruct.2011.08.014.
- [24] T. T. H. Nguyen, B. Bary, and T. de Larrard, “Coupled carbonation-rust formation-damage modeling and simulation of steel corrosion in 3D mesoscale reinforced concrete,”

- Cement and Concrete Research*, vol. 74, pp. 95–107, Aug. 2015, doi: 10.1016/j.cemconres.2015.04.008.
- [25] A. Jamali, U. Angst, B. Adey, and B. Elsener, “Modeling of corrosion-induced concrete cover cracking: A critical analysis,” *Construction and Building Materials*, vol. 42, pp. 225–237, 2013. doi: 10.1016/j.conbuildmat.2013.01.019.
- [26] I. Fernandez and C. G. Berrocal, “Mechanical Properties of 30 Year-Old Naturally Corroded Steel Reinforcing Bars,” *International Journal of Concrete Structures and Materials*, vol. 13, no. 1, Dec. 2019, doi: 10.1186/s40069-018-0308-x.
- [27] Y. G. Du, L. A. Clark, and A. H. C. Chan, “Residual capacity of corroded reinforcing bars.”
- [28] Y. Zhao, Y. Wu, and W. Jin, “Distribution of millscale on corroded steel bars and penetration of steel corrosion products in concrete,” *Corrosion Science*, vol. 66, pp. 160–168, Jan. 2013, doi: 10.1016/j.corsci.2012.09.014.
- [29] D. Vořechovská, M. Vořechovský, V. Ž. Konstrucích, and I. D. Vořechovská, “Sborník vědeckých prací Vysoké školy báňské-Technické univerzity Ostrava ANALYTICAL AND NUMERICAL APPROACHES TO MODELLING OF REINFORCEMENT CORROSION IN CONCRETE ANALYTICKÉ A NUMERICKÉ PŘÍSTUPY PRO MODELOVÁNÍ KOROZE.”
- [30] K. Zhang, J. Xiao, Y. Zhao, and Q. Zhang, “Analytical model for critical corrosion level of reinforcements to cause the cracking of concrete cover,” *Construction and Building Materials*, vol. 223, pp. 185–197, Oct. 2019, doi: 10.1016/j.conbuildmat.2019.06.210.
- [31] X. Du and L. Jin, “Meso-scale numerical investigation on cracking of cover concrete induced by corrosion of reinforcing steel,” *Engineering Failure Analysis*, vol. 39, pp. 21–33, Apr. 2014, doi: 10.1016/j.engfailanal.2014.01.011.
- [32] G. S. Duffó, W. Morris, I. Raspini, and C. Saragovi, “A study of steel rebars embedded in concrete during 65 years,” *Corrosion Science*, vol. 46, no. 9, pp. 2143–2157, Sep. 2004, doi: 10.1016/j.corsci.2004.01.006.
- [33] Y. R. Alharbi, M. Galal, A. A. Abadel, and M. Kohail, “Bond behavior between concrete and steel rebars for stressed elements,” *Ain Shams Engineering Journal*, vol. 12, no. 2, pp. 1231–1239, Jun. 2021, doi: 10.1016/j.asej.2020.10.001.
- [34] A. A. Almusallam, A. S. Al-Gahtani, and A. Rauf Aziz, “Effect of reinforcement corrosion on bond strength,” 1996.
- [35] W. Zhu, R. François, D. Coronelli, and D. Cleland, “Effect of corrosion of reinforcement on the mechanical behaviour of highly corroded RC beams,” *Engineering Structures*, vol. 56, pp. 544–554, Nov. 2013, doi: 10.1016/j.engstruct.2013.04.017.
- [36] L. C. Bank, *Composites for Construction: Structural Design with FRP Materials*. 2007. doi: 10.1002/9780470121429.

- [37] R. H. Haddad, “Hybrid repair configurations with CFRP composites for recovering structural performance of steel-corroded beams,” *Construction and Building Materials*, vol. 124, pp. 508–518, Oct. 2016, doi: 10.1016/j.conbuildmat.2016.07.124.
- [38] B. Fu, J. G. Teng, J. F. Chen, G. M. Chen, and Y. C. Guo, “Concrete Cover Separation in FRP-Plated RC Beams: Mitigation Using FRP U-Jackets,” *Journal of Composites for Construction*, vol. 21, no. 2, p. 04016077, Apr. 2017, doi: 10.1061/(asce)cc.1943-5614.0000721.
- [39] B. Fu, X. T. Tang, L. J. Li, F. Liu, and G. Lin, “Inclined FRP U-jackets for enhancing structural performance of FRP-plated RC beams suffering from IC debonding,” *Composite Structures*, vol. 200, pp. 36–46, Sep. 2018, doi: 10.1016/j.compstruct.2018.05.074.
- [40] W. Chen, T. M. Pham, H. Sicheembe, L. Chen, and H. Hao, “Experimental study of flexural behaviour of RC beams strengthened by longitudinal and U-shaped basalt FRP sheet,” *Composites Part B: Engineering*, vol. 134, 2018, doi: 10.1016/j.compositesb.2017.09.053.
- [41] W. Zhu, R. François, D. Coronelli, and D. Cleland, “Effect of corrosion of reinforcement on the mechanical behaviour of highly corroded RC beams,” *Engineering Structures*, vol. 56, 2013, doi: 10.1016/j.engstruct.2013.04.017.
- [42] Per Kettil, “<https://www.sbuf.se/Projektsida?project=dcbeae58-a29d-4172-afc7-672e70d640ab>,” Sep. 15, 2018.
- [43] Fédération internationale du béton., *Fib model code for concrete structures 2010*.
- [44] Jan Gerrit Rots, “Computational Modeling of Concrete Fracture,” 1988.
- [45] F. J. Vecchio and M. P. Collins, “Compression Response of Cracked Reinforced Concrete,” *Journal of Structural Engineering*, vol. 119, no. 12, 1993, doi: 10.1061/(asce)0733-9445(1993)119:12(3590).
- [46] H. A. W. Cornelissen, D. A. Hordijk, and H. W. Reinhardt, “EXPERIMENTAL DETERMINATION OF CRACK SOFTENING CHARACTERISTICS OF NORMALWEIGHT AND LIGHTWEIGHT CONCRETE.,” *Heron*, vol. 31, no. 2, 1985.
- [47] P. H. Feenstra and R. de Borst, “Aspects of robust computational modeling for plain and reinforced concrete,” *Heron*, vol. 38, no. 4, 1993.
- [48] Belletti *et al.*, “Validation of the Guidelines for Nonlinear Finite Element Analysis of Concrete Structures. Part: Slabs,” Jun. 2017.
- [49] Hendriks, Max A.N, de Boer, Ane, Belletti, and Beatrice, “Guidelines for nonlinear finite element analysis of concrete structures: Girder Members,” 2012.
- [50] R. Kalfat and R. Al-Mahaidi, “Numerical and Experimental Validation of FRP Patch Anchors Used to Improve the Performance of FRP Laminates Bonded to Concrete,”

*Journal of Composites for Construction*, vol. 18, no. 3, 2014, doi: 10.1061/(asce)cc.1943-5614.0000437.

- [51] M. Blomfors, C. G. Berrocal, K. Lundgren, and K. Zandi, “Incorporation of pre-existing cracks in finite element analyses of reinforced concrete beams without transverse reinforcement,” *Engineering Structures*, vol. 229, 2021, doi: 10.1016/j.engstruct.2020.111601.
- [52] M. Blomfors, K. Lundgren, and K. Zandi, “Incorporation of pre-existing longitudinal cracks in finite element analyses of corroded reinforced concrete beams failing in anchorage,” *Structure and Infrastructure Engineering*, 2020, doi: 10.1080/15732479.2020.1782444.
- [53] F. H. Wittmann, K. Rokugo, E. Brühwiler, H. Mihashi, and P. Simonin, “Fracture energy and strain softening of concrete as determined by means of compact tension specimens,” *Materials and Structures*, vol. 21, no. 1, 1988, doi: 10.1007/BF02472525.
- [54] X. Z. Lu, J. G. Teng, L. P. Ye, and J. J. Jiang, “Bond-slip models for FRP sheets/plates bonded to concrete,” *Engineering Structures*, vol. 27, no. 6, 2005, doi: 10.1016/j.engstruct.2005.01.014.

## 9. Appendix

### Appendix A: Material properties of reinforcement

Table A-1: The material properties of steel reinforcement determined through tensile tests conducted by Yang [8].

Reinforcement rebars	$E_s$ [GPa]	$f_{sy}$ [MPa]	$f_{su}$ [MPa]	$\epsilon_{su}$ (%)
Compression rebars, $\phi 10$	191	570	661	8.1
Tensile rebars, $\phi 12$	200	528	630	8.9
Stirrups, $\phi 8$	202	531	654	9.6

$E_s$  - Elastic modulus

$f_{sy}$  - Yield strength

$f_{su}$  - Ultimate tensile strength

$\epsilon_{su}$  - Ultimate tensile strain

Table A-2: Values for the stress-strain curve of rebars used as input in the analyzes.

Compression rebars			Tensile rebars			Stirrups		
$\sigma$ [MPa]	$\epsilon$ [%]	$E$ [GPa]	$\sigma$ [MPa]	$\epsilon$ [%]	$E$ [GPa]	$\sigma$ [MPa]	$\epsilon$ [%]	$E$ [GPa]
0	0	191	0	0	200	0	0	202
530	0.298	-	505	0.3	-	531	0.26	-
570	0.5	-	530	0.5	-	654	9.6	-
605	1.5	-	560	1.3	-	-	-	-
635	2.78	-	590	2.5	-	-	-	-
661	8.1	-	620	5	-	-	-	-
650	12	-	630	8.9	-	-	-	-
0	12.01	-	625	12	-	-	-	-

$\sigma$  - Tensile strength

$\epsilon$  - Tensile strain

$E$  - Elastic modulus

## Appendix B: Pre-loading and corrosion-induced cracks

### Case A

The stress-strain relationship for pre-loading and corrosion-induced cracks are presented in Table B-1. The mesh size of 20 mm was used to calculate the strain values. The coordinates of pre-loading cracks and their crack widths are presented in Table B-2.

### Pre-loading cracks

Table B-1: Stress-strain relationship for pre-loading cracks for Case A.

Crack 1		Cracks 2, 5 and 6		Cracks 3 and 4	
$\sigma$ [MPa]	$\epsilon$ [%]	$\sigma$ [MPa]	$\epsilon$ [%]	$\sigma$ [MPa]	$\epsilon$ [%]
0	0	0	0	0	0
2.5	7.51E-05	0.695	2.09E-05	0.001	3.00E-08
0	7.32E-03	0	4.47E-03	0	6.43E-06

Table B-2: The position and the width of pre-loading cracks for Case A.

Crack number	x coordinate [mm]	Crack width [mm]
1	758	0.013
2	865	0.054
3	942	0.131
4	1075	0.172
5	1224	0.070
6	1350	0.070

### Corrosion-induced crack

Table B-3: Stress-strain relationship for corrosion-induced cracks for Case A and B.

Corrosion-induced crack	
$\sigma$ [MPa]	$\epsilon$ [%]
0	0
0.001	3.00E-08
0	6.43E-06

## **Case B**

The stress-strain relationship for pre-loading cracks is presented in Table B-4. The stress-strain relationship for the corrosion-induced crack was chosen to be the same as for Case A, which is presented in Table B-3.

Table B-4: Stress-strain relationship for pre-loading cracks for Case B.

<b>Pre-loading cracks</b>	
<b><math>\sigma</math> [MPa]</b>	<b><math>\epsilon</math> [%]</b>
0	0
2.5	7.51E-05
0	7.32E-03

## Appendix C: Corrosion modelling

The position and corrosion level of pits for Case A and B are presented in this section.

Table C-1: The positions and corrosion level of pits in Case A.

<b>Pits in Case A</b>				
<b>Bar/pit</b>	<b>Yield length [mm]</b>	<b>X Coordinate [mm]</b>	<b>Corrosion level [mm]</b>	<b>Rebar area [mm<sup>2</sup>]</b>
Ia	20	910-930	55	49.5
Ib	40	930-970	48	57.2
Ic	10	1220-1230	55	49.5
IIa	20	885-905	55	49.5
IIb	20	1210-1230	43	47.3

All the pits for Case B have the same yield length, corrosion level and rebar area as pit Ib in Case A.

Table C-2: The positions of pits in Case B.

<b>Pits in Case B</b>	
<b>Bar/pit</b>	<b>X- Coordinate [mm]</b>
Ia, Xa	1.424-1.464
Ib, Xb	2.074-2.114
Ic, Xc	2.594-2.634
IIa, IXa	0.904-0.944
IIb, IXb	1.684-1.724
IIc, IXc	3.114-3.154
IIIa, VIIIa	1.164-1.204
IIIb, VIIIb	2.334-2.374
IIIc, VIIIc	2.724-2.764
IVa, VIIa	1.424-1.464
IVb, VIIb	1.814-1.854
IVc, VIIc	2.984-3.024
Va, VIa	0.774-0.814
Vb, VIb	3.244-3.284

## Appendix D: FRP properties

The stress-strain properties for the individual FRP components and the interface properties are presented in this section.

Table D-1: Stress-strain values for different FRP components used as input in the analyzes

FRP plate		Inclined U-jackets		Vertical U-jackets (x- direction)		Vertical U-jackets (y-direction)	
Stress [MPa]	Strain [%]	Stress [MPa]	Strain [%]	Stress [MPa]	Strain [%]	Stress [MPa]	Strain [%]
2717.80	1.27	714.24	1.24	714.24	1.24	88.04	1.24

Table D-2: Non-linear interface properties for FRP to concrete interface and FRP to FRP interface

FRP to concrete/FRP bond interface	
Bond stress ( $\tau$ ) [MPa]	Slip (s) [mm]
0	0
5.74	0.07
0	0.182

Table D-3: Linear interface properties for the different FRP components used in modelling.

Linear interface properties for FRP	
Shear stiffness modules in x-direction	$2.11 \cdot 10^{11}$ [N/m <sup>3</sup> ]
Shear stiffness modules in y-direction	$2.11 \cdot 10^{11}$ [N/m <sup>3</sup> ]
Normal stiffness modules in z-direction	$3.55 \cdot 10^{12}$ [N/m <sup>3</sup> ]

## Appendix E: Hand calculation for Case B

### Input data

$b := 150\text{mm}$	Width
$h := 225\text{mm}$	Height
$L := 4200\text{mm}$	Length
$\phi_{\text{top}} := 10\text{mm}$	Diameter of the top rebars
$\phi_{\text{bottom}} := 12\text{mm}$	Diameter of the bottom rebars
$\phi_{\text{stirrup}} := 8\text{mm}$	Diameter of the stirrups
$d_{\text{c.ref}} := 24\text{mm}$	Clear concrete cover of tensile bars
$d_{\text{efl}} := h - d_{\text{c.ref}} = 201\text{mm}$	
$L_{\text{ef}} := L - 300\text{mm} = 3.9 \times 10^3\text{mm}$	Distance between supports
$A := b \cdot h = 0.034\text{m}^2$	Area of beam

### Concrete parameters

$f_{\text{cm}} := 0.8 \cdot 78.7\text{MPa} = 62.96\text{MPa}$	Concrete compressive strength
$f_{\text{ctm}} := 4.21\text{MPa}$	Concrete mean tensile strength
$E_{\text{cm}} := 33.3\text{GPa}$	Elastic modulus of the concrete
$\varepsilon_{\text{cu}} := 0.0035$	Ultimate strain

## Reinforcement properties

$$f_{sy.bottom} := 570\text{MPa}$$

Yield strength of the tensile rebars

$$E_{s.bottom} := 191\text{GPa}$$

Elastic modulus of tensile rebars

$$f_{su.bottom} := 661\text{MPa}$$

Ultimate capacity of the tensile rebars

$$f_{sy.top} := 528\text{MPa}$$

Yield capacity of the compressive rebars

$$E_{s.top} := 200\text{GPa}$$

Elastic modulus of the compressive rebars

$$f_{su.top} := 630\text{MPa}$$

Ultimate capacity of the compressive rebars

$$\epsilon_{su.bottom} := 0.12$$

Ultimate strain of the tensile rebars

$$\epsilon_{sy.bottom} := \frac{f_{sy.bottom}}{E_{s.bottom}} = 2.984 \times 10^{-3}$$

Yielding strain of the tensile rebars

$$n_{s.top} := 2$$

No. of compressive bars

$$n_{s.bottom} := 2$$

No. of tensile bars

$$A_{s.bottom} := \frac{\pi \cdot \phi_{bottom}^2}{4} = 113.097 \cdot \text{mm}^2$$

Area of 1 tensile rebar

$$A_{s.top} := \frac{\pi \cdot \phi_{top}^2}{4} = 78.54 \cdot \text{mm}^2$$

Area of 1 compressive rebar

$$A_s := n_{s.bottom} \cdot A_{s.bottom} = 226.195 \cdot \text{mm}^2$$

Total tensile steel area

$$\rho := \frac{A_s}{b \cdot (d_{efl})} = 7.502 \times 10^{-3}$$

Reinforcement ratio for Case A

## Design of cross section Case B

### New cross section from minimum cover and rebar spacing:

$$d1 := 49\text{mm}$$

Effective cover for tensile bars

$$n := 10$$

No. of bars in tensile zone

$$n_{\text{top}} := 2$$

No. of bars in compression zone

$$c_{\text{min}} := 35\text{mm}$$

Minimum concrete cover

$$s_{\text{min}} := 45\text{mm}$$

Spacing between bars

### **Width of beam**

$$B := 2 \cdot \phi_{\text{stirrup}} + s_{\text{min}} \cdot (n - 1) + \phi_{\text{bottom}} + 2 \cdot c_{\text{min}} = 503 \cdot \text{mm}$$
 Width of new cross section

$$A_{s,\text{new}} := n \cdot A_{s,\text{bottom}} = 1.131 \times 10^3 \cdot \text{mm}^2$$

Area of tensile bars

$$A_{c,\text{new}} := \frac{A_{s,\text{new}}}{\rho} = 0.151 \text{m}^2$$

The new area of cross-section calculated by keeping the same  $\rho$  as in Case A.

### **Height of beam**

$$H := \frac{A_{c,\text{new}}}{B} = 299.702 \cdot \text{mm}$$

Beam height

$$\frac{B}{H} = 1.678$$

Width / height ratio

$$\frac{L}{H} = 14.014$$

Limit is  $L/H < 20$

$$d := H - d1 = 0.251 \text{m}$$

Depth of beam from compressive side to centre of tensile rebars

$$d2 := 48\text{mm}$$

Effective cover of the compressive rebars

$$L_p := \frac{L_{ef}}{3} = 1.3 \times 10^3 \cdot \text{mm}$$

Distance from centre of support to the loading plate

$$I := \frac{B \cdot H^3}{12} = 1.128 \times 10^{-3} \cdot \text{m}^4$$

Moment of inertia

### Cracking moment

$$M_{cr} := \frac{f_{ctm} \cdot I}{\frac{H}{2}} = 31.701 \cdot \text{kN} \cdot \text{m}$$

Cracking moment

$$P_{cr} := \frac{M_{cr}}{L_p} = 24.386 \cdot \text{kN}$$

Cracking point load

$$P_{cr,T} := 2 \cdot P_{cr} = 48.771 \cdot \text{kN}$$

Total cracking load

$$\alpha := \frac{E_{s,\text{bottom}}}{E_{cm}} = 5.736$$

Modular ratio

### **Sectional constants for uncracked section**

$$A_I := B \cdot H + (\alpha - 1) \cdot A_{s,\text{new}} + (\alpha - 1) \cdot (n_{\text{top}} \cdot A_{s,\text{top}}) = 0.157 \text{ m}^2$$

$$x_I := \frac{B \cdot H \cdot \frac{H}{2} + (\alpha - 1) A_{s,\text{new}} \cdot d + (\alpha - 1) \cdot (n_{\text{top}} \cdot A_{s,\text{top}}) \cdot d_2}{A_I} = 0.153 \text{ m}$$

Guess  $x$                        $x_1 := 200 \text{ mm}$

$$x_1 := \text{root} \left[ \frac{B \cdot x_1^2}{2} + (\alpha - 1) \cdot 2 \cdot A_{s,\text{top}} \cdot (x_1 - d_2) - \alpha \cdot A_{s,\text{new}} \cdot (d - x_1), x_1 \right] = 68.178 \cdot \text{mm}$$

$$I_{I,ef} := \frac{B \cdot x_1^3}{3} + (\alpha - 1) \cdot 2 \cdot A_{s,\text{top}} \cdot (x_1 - d_2)^2 + \alpha \cdot A_{s,\text{new}} \cdot (d - x_1)^2 = 2.696 \times 10^{-4} \text{ m}^4$$

**Moment and load when yielding starts**

$$\alpha_R := 0.5$$

$$\beta_R := \frac{1}{3}$$

$$\epsilon_{cc} := \frac{\epsilon_{sy, \text{bottom}}}{d - x} \cdot (0 - x) \quad \text{Concrete compressive strain}$$

$$\epsilon_{s, \text{top}} := \frac{\epsilon_{sy, \text{bottom}}}{d - x_y} \cdot (d_2 - x) \quad \text{Compressive rebar strain}$$

$$F_{sy} := f_{sy, \text{bottom}} \cdot n \cdot A_{s, \text{bottom}} = 644.655 \cdot \text{kN}$$

$$F_c := \alpha_R \cdot E_{cm} \cdot \epsilon_{cc} \cdot b \cdot x \quad \text{Force in concrete}$$

$$F_{s, \text{top}} := E_{s, \text{top}} \cdot \epsilon_{s, \text{top}} \cdot n_{\text{top}} \cdot A_{s, \text{top}} \quad \text{Force in compressive rebars}$$

$$(F_{sy} + F_c + F_{s, \text{top}}) = 0 \quad \text{Equilibrium condition}$$

Guess  $x_y := 80 \text{ mm}$

$$x_y := \text{root} \left[ \begin{array}{l} F_{sy} + \alpha_R \cdot E_{cm} \cdot \frac{\epsilon_{sy, \text{bottom}}}{d - x_y} \cdot (0 - x_y) \cdot B \cdot x_y \dots, x_y \\ + E_{s, \text{top}} \cdot \left[ \frac{\epsilon_{sy, \text{bottom}}}{d - x_y} \cdot (d_2 - x_y) \cdot n_{\text{top}} \cdot A_{s, \text{top}} \right] \end{array} \right] = 68.081 \cdot \text{mm}$$

$$x_y = 68.081 \cdot \text{mm} \quad \text{Neutral axis when yielding starts}$$

$$\epsilon_{cc} := \frac{\epsilon_{sy, \text{bottom}}}{d - x_y} \cdot (0 - x_y) = -1.113 \times 10^{-3}$$

$$\epsilon_{s, \text{top}} := \frac{\epsilon_{sy, \text{bottom}}}{d - x_y} \cdot (d_2 - x_y) = -3.282 \times 10^{-4}$$

$$F_c := \alpha_R \cdot E_{cm} \cdot \frac{\epsilon_{sy, \text{bottom}}}{d - x_y} \cdot (0 - x_y) \cdot B \cdot x_y = -634.346 \cdot \text{kN}$$

$$F_{s, \text{top}} := E_{s, \text{top}} \cdot \left[ \frac{\epsilon_{sy, \text{bottom}}}{d - x_y} \cdot (d_2 - x_y) \cdot n_{\text{top}} \cdot A_{s, \text{top}} \right] = -10.309 \cdot \text{kN}$$

### Yielding moment

$$M_y := F_c \cdot (\beta_R \cdot x_y - d) + F_{s,top} \cdot (d_2 - d) = 146.726 \cdot \text{kN} \cdot \text{m} \quad \text{Moment equilibrium around bottom rebar}$$

$$P_y := \frac{M_y}{L_p} = 112.866 \cdot \text{kN} \quad \text{For one point load causing } M_y$$

$$P_{y,T} := 2 \cdot P_y = 225.732 \cdot \text{kN} \quad \text{Total yielding force}$$

### Behaviour in Ultimate state

For rectangular distribution (EC2-1-1 3.1.7(3))

$$\lambda := 0.8 \quad \eta := 1$$

$$\epsilon_{cc,u} := -\epsilon_{cu} = -3.5 \times 10^{-3}$$

### Calculating height of compression zone

Guess  $x_u := 70 \text{ mm}$

$$x_u := \text{root} \left[ f_{su,bottom} \cdot A_{s,bottom} \cdot n - \eta \cdot f_{cm} \cdot \lambda \cdot x_u \cdot B - E_{s,top} \cdot \left[ \frac{\epsilon_{cc,u}}{x_u} \cdot (d_2 - x_u) \right] \cdot A_{s,top} \cdot x_u \right] = 0.031 \text{ m}$$

### Control strain of rebars

$$\epsilon_{s,b,u} := \frac{\epsilon_{cc,u}}{0 - x_u} \cdot (d - x_u) = 0.025 \quad \text{Strain in tensile rebar}$$

$$\epsilon_{sy,bottom} = 2.984 \times 10^{-3}$$

$$\epsilon_{s,t,u} := \frac{\epsilon_{cc,u}}{0 - x_u} \cdot (d_2 - x_u) = 1.967 \times 10^{-3} \quad \text{Strain in compressive rebar}$$

### Ultimate moment

$$M_u := \eta \cdot f_{cm} \cdot B \cdot \lambda \cdot x_u \cdot (x_u - \lambda \cdot x_u \cdot 0.5) + A_{s,top} \cdot n_{top} \cdot E_{s,top} \cdot \epsilon_{s,t,u} \cdot (d_2 - x_u) \dots = 179.867 \cdot \text{kN} \cdot \text{m} \\ + A_{s,bottom} \cdot n \cdot f_{su,bottom} \cdot (d - x_u)$$

$$P_u := \frac{M_u}{L_p} = 138.359 \cdot \text{kN}$$

$$P_{u,T} := 2 \cdot P_u = 276.719 \cdot \text{kN}$$

Total Ultimate load

### Calculation of max crack spacing

$$C := c_{\min} + \phi_{\text{stirrup}} = 43 \cdot \text{mm}$$

$$k_1 := 0.8$$

$$k_2 := 0.5$$

$$k_3 := 3.4$$

$$k_4 := 0.425$$

$$\phi := 12 \text{mm}$$

$$h_{c,\text{eff}} := \frac{(H - x_u)}{3} = 89.658 \cdot \text{mm} \quad \text{Minimum of the 3 equations to the right}$$

$$\frac{H}{2} = 149.851 \cdot \text{mm}$$

$$2.5 \cdot (H - d) = 122.5 \cdot \text{mm}$$

$$\frac{(H - x_u)}{3} = 89.658 \cdot \text{mm}$$

$$A_{c,\text{eff}} := h_{c,\text{eff}} \cdot B = 4.51 \times 10^4 \cdot \text{mm}^2$$

$$\rho_{p,\text{eff}} := \frac{n \cdot A_{s,\text{bottom}}}{A_{c,\text{eff}}} = 0.025$$

$$S_{r,\text{max}} := k_3 \cdot C + \frac{k_1 \cdot k_2 \cdot k_4 \cdot \phi}{\rho_{p,\text{eff}}} = 227.546 \cdot \text{mm}$$

Max spacing between cracks

$$S_{r,\text{mean}} := \frac{S_{r,\text{max}}}{1.7} = 133.851 \cdot \text{mm}$$

Choose mean crack spacing as 130 mm

### Cracked span length of the beam

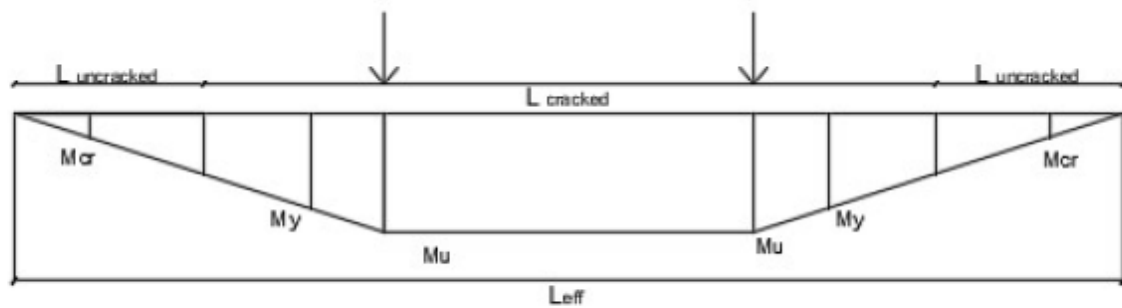
$$L_{\text{uncracked}} := \frac{\frac{L_{\text{ef}}}{3} \cdot \frac{P_{\text{cr.T}} + P_{\text{y.T}}}{2}}{P_{\text{u.T}}} = 0.645 \text{ m}$$

$$L_{\text{cracked}} := L_{\text{ef}} - 2 \cdot L_{\text{uncracked}} = 2.61 \text{ m}$$

### Number of cracks

$$N_{\text{cracks}} := \frac{L_{\text{cracked}}}{S_{\text{r.mean}}} = 19.502$$

Assume 21 cracks as simplification  
with 130 mm spacing



**Shear control:**

$$V_{Ed} := P_u = 138.359 \cdot \text{kN}$$

$$f_{ck} := f_{cm} - 8 \text{MPa} = 54.96 \text{MPa}$$

$$f_{cd} := \frac{f_{ck}}{1.5} = 36.64 \text{MPa}$$

**Check 1**  $V_{Rd} := 0.5v \cdot f_{cd} \cdot b \cdot d$  ■

$$v := 0.6 \left( 1 - \frac{f_{ck}}{250 \text{MPa}} \right) = 0.468$$

$$V_{Rd} := 0.5v \cdot f_{cd} \cdot B \cdot d = 1.081 \times 10^3 \cdot \text{kN} \quad V_{Rd} > V_{Ed} \quad \text{OK!}$$

**Check 2**  $V_{Rd.c} := C_{Rd.c} \cdot k \cdot (100\rho_l f_{ck})^{\frac{1}{3}} \cdot B \cdot d$  ■

$$C_{Rd.c} := \frac{0.18}{1.5} = 0.12$$

$$k := \min \left( 2.0, 1 + \sqrt{\frac{200 \text{mm}}{d}} \right) = 1.893$$

$$\rho_l := \frac{n \cdot A_{s, \text{bottom}}}{B \cdot d} = 8.969 \times 10^{-3}$$

$$V_{Rd.c, \text{min}} := 0.035 \cdot k^{\frac{3}{2}} \cdot \left( \frac{f_{ck}}{\text{MPa}} \right)^{\frac{1}{2}} \cdot 1 \text{MPa} \cdot B \cdot d = 85.232 \cdot \text{kN}$$

$$V_{Rd.c} := C_{Rd.c} \cdot k \cdot \left[ 100\rho_l \left( \frac{f_{ck}}{\text{MPa}} \right) \right]^{\frac{1}{3}} \cdot B \cdot d \cdot 1 \text{MPa} = 105.04 \cdot \text{kN}$$

$V_{Rd.c} < V_{Ed}$       There is need for stirrups

### Calculation of the spacing

$$\theta := 35$$

The angle for shear crack

$$\cot\theta := 1.43$$

$$f_{ywd} := 500 \text{ MPa}$$

$$A_{sw} := 2\pi \cdot \frac{\phi_{stirrup}^2}{4} = 1.005 \times 10^{-4} \text{ m}^2$$

Area of stirrups

$$s_w := 0.9 \cdot d \cdot A_{sw} \cdot \cot\theta \cdot \frac{f_{ywd}}{V_{Ed}} = 117.219 \text{ mm}$$

Spacing between stirrups

$$s_{max} := 0.75 \cdot d = 188.026 \text{ mm}$$

Max spacing

Chose Spacing to be 100 mm

### **Number of stirrups:**

$$n_{stirrup} := \frac{L_{ef}}{3 \cdot s} = 11.09$$

Chose 13

With spacing of 100 mm

### Calculation of the crack width in SLS:

$$M_{sls} := \frac{1}{1.5} \cdot M_y = 97.817 \text{ kN}\cdot\text{m}$$

Assumed based on coefficient  $\phi$  for imposed load in ULS and SLS

### **Calculation of neutral axis in SLS:**

$$\text{Guess } x1 := 78.771 \text{ mm}$$

$$x := \frac{B \cdot \frac{x1^2}{2} + (\alpha - 1) \cdot (n_{top} \cdot A_{s,top}) \cdot d2 + \alpha \cdot A_{s,new} \cdot d}{B \cdot x1 + n_{top} \cdot A_{s,top} + A_{s,new}} = 78.771 \text{ mm}$$

$$I_{sls} := \frac{B \cdot x^3}{3} + (\alpha - 1) \cdot n_{top} \cdot A_{s,top} \cdot (x - d2)^2 + \alpha \cdot A_{s,new} \cdot (d - x)^2 = 2.744 \times 10^{-4} \text{ m}^4$$

$$\sigma_c := \frac{M_{sls}}{I_{sls}} \cdot (x1 - x) = -1.222 \times 10^{-4} \text{ MPa}$$

Stress at neutral axis

### Calculation of the steel stress:

$$\sigma_{\text{concrete}} := \frac{M_{\text{sls}}}{I_{\text{sls}}} \cdot (d - x) = 61.287 \cdot \text{MPa}$$

Concrete stress at steel level

$$\sigma_{\text{steel}} := \alpha \cdot \sigma_{\text{c}} = 351.525 \cdot \text{MPa}$$

Stresses at the steel

$$k_t := 0.6$$

Short term loading

$$\rho_{\text{p.ef}} := \frac{A_{\text{s.new}}}{B \cdot x} = 0.029$$

$$\varepsilon_{\text{crack}} := \frac{\sigma_{\text{steel}} - k_t \cdot \frac{f_{\text{ctm}}}{\rho_{\text{p.ef}}} \cdot (1 + \alpha \cdot \rho_{\text{p.ef}})}{E_{\text{s.bottom}}} = 1.301 \times 10^{-3}$$

$$w := S_{\text{r.max}} \cdot \varepsilon_{\text{crack}} = 0.296 \cdot \text{mm}$$

The resulting crack width

$$\sigma_s := 0.25 \cdot f_{\text{ctm}} = 1.053 \cdot \text{MPa}$$

$$G_f := 134 \frac{\text{N}}{\text{m}}$$

Fracture energy

$$w_s := 0.75 \cdot \frac{G_f}{f_{\text{ctm}}} = 0.024 \cdot \text{mm}$$

$$w_{\text{ult}} := 5 \cdot \frac{G_f}{f_{\text{ctm}}} = 0.159 \cdot \text{mm}$$

Ultimate crack width

$$w := 0.99 \cdot w_{\text{ult}} = 1.576 \times 10^{-4} \cdot \text{m}$$

Chosen crack width

$$h_{\text{mesh}} := 20 \text{mm}$$

Mesh size

$$f_{\text{ctm.c}} := \frac{(w_{\text{ult}} - w) \cdot \sigma_s}{(w_{\text{ult}} - w_s)} = 0.012 \cdot \text{MPa}$$

The remaining tensile strength

$$\varepsilon_{\text{ctm.c}} := \frac{f_{\text{ctm.c}}}{E_{\text{cm}}} = 3.718 \times 10^{-7}$$

The correspond strain

$$\varepsilon_{\text{c.0}} := \frac{(w_{\text{ult}} - w)}{h_{\text{mesh}}} = 7.957 \times 10^{-5}$$

The maximum strain